Experimental Investigation of Short and Slender Rectangular Concrete Columns Reinforced with GFRP Bars under Eccentric Axial Loads

Koosha Khorramian[1] and Pedram Sadeghian[2], M.ASCE

ABSTRACT: In this paper, the experimental behavior of short and slender concrete columns reinforced with glass fiber-reinforced polymer (GFRP) bars under eccentric compression loading is presented. A total of ten large-scale concrete column specimens with a rectangular cross-section (205×306 mm) were tested under single curvature condition with equal load eccentricities at both ends of the column. Four slenderness ratios of 16.6, 21.5, 39.7, and 59.5 and two reinforcement ratios of 2.78% and 4.80% were considered. The results showed that no crushing of GFRP bars occurred prior to concrete spalling. The columns were able to sustain load, moment, and deformation after the concrete spalling up to the crushing of GFRP bars in compression. The latter was attributed to the contribution of GFRP bars in compression. An analytical model was also adopted to predict the behavior of the test specimens and to evaluate the effect of load eccentricities beyond of the one considered in the experimental program. Also, the flexural stiffness and moment magnification factor obtained from the experimental program were compared with those calculated using equations from the literature. The results showed that most of the equations underestimated the flexural stiffness and the magnified moment.

DOI: 10.1061/(ASCE)CC.1943-5614.0001088

[1] PhD Candidate, Department of Civil and Resource Engineering, Dalhousie University, D301, 1360 Barrington street, Halifax, NS, B3H 4R2 Canada, koosha.khorramian@dal.ca (corresponding author)
[2] Associate Professor and Canada Research Chair in Sustainable Infrastructure, Department of Civil and Resource Engineering, Dalhousie University, D403, 1360 Barrington Street, Halifax, NS, B3H 4R2 Canada, Pedram.Sadeghian@dal.ca

KEYWORDS: GFRP bar, slender concrete columns, eccentric loading, rectangular section, experimental, GFRP crushing, flexural stiffness, moment magnification.

INTRODUCTION

The interest in using fiber-reinforced polymer (FRP) bars as an alternative to steel reinforcing bars in concrete structures has been increasing due to the superior characteristics of FRPs such as high corrosion resistance, high tensile strength, and their electromagnetic transparency. Among structural members, FRP-reinforced concrete (RC) columns have been treated with extra caution. Currently, ACI 440.1R-15 (2015) guideline does not consider FRP bars in compression for reinforcing concrete columns due to a lack of research data. However, the guideline is in the process of being converted into an accompanied code to ACI 318-19 (2019) for glass FRP (GFRP) reinforced concrete (GFRP-RC) members and the inclusion of both short and slender GFRP-RC concrete columns in under consideration. For GFRP-RC columns, a critical slenderness ratio of 17 is under consideration form a numerical study performed by Mirmiran et al. (2001) which is lower than the limit of 22 defined for conventional steel-RC columns per ACI 318-19 (2019). The latter shows that FRP-RC columns are more susceptible to be categorized as slender columns in comparison with steel-RC columns. In fact, the lack of experimental data on the behavior of slender FRP-RC columns can lead to conservative decision making. There have been many studies on the behavior of short GFRP-RC columns (Pantelides et al., 2013; Afifi et al., 2014; Mohamed et al., 2014; Guérin et al., 2018a and 2018b; Hadhood et al., 2019). Different concrete types (Elchalakani et al., 2018; Salah-Eldin et al., 2019), different loading conditions (Maranan et al., 2016; Hadhood et al., 2016; Hadi et al., 2016; Sun et al., 2017), and different cross-sections

(AlAjarmeh et al., 2019a and 2019b; AlAjarmeh et al., 2020a and 2020b) were considered. However, the studies on the behavior of slender GFRP-RC columns have been very limited (Tikka et al., 2010; Hales et al., 2016; Maranan et al., 2016; Elchalakani and Ma, 2017; Xue et al., 2018; Khorramian and Sadeghian, 2019a; Abdelazim et al., 2020a).

Tikka et al. (2010) conducted an experimental study on eight square GFRP-RC columns with a width of 150 mm, slenderness ratio of 41.6, reinforcement ratios of 2.3 and 3.4%, and eccentricity-to-column width ratios of 0.2, 0.4, 0.6, and 0.8. The study showed that specimens tolerated considerable displacement before failure. Hales et al. (2016) studied the behavior of circular GFRP-RC columns, in which six slender columns with a slenderness ratio of 49 were tested with two different eccentricities. It was observed that for 8.3% and 33% eccentricity-to-column diameter ratios, the failure was governed by material failure and global buckling, respectively. It was reported that the system of GFRP bars and GFRP spirals is a viable system for slender columns. Maranan et al. (2016) tested two slender circular GFRP-RC columns (geopolymer concrete) with a slenderness ratio of 32, a diameter of 250 mm, and a reinforcement ratio of 2.43%. It was observed that the slender columns were failed at a load of 66% and 82% of the strength of their short-column counterparts. Elchalakani and Ma (2017) tested seven rectangular GFRP-RC columns (160×260 mm) with a slenderness ratio of 26, eccentricities of 0, 25, 35, and 45 mm and with a reinforcement ratio of 1.83%. It was observed that the average increase in the capacity of GFRP-RC specimens was 3.2% with respect to plain concrete section capacity. Xue et al. (2018) tested fifteen slender rectangular GFRP-RC columns with a width of 300 mm. The slenderness ratios of 20.8, 27.7, 34.6, and 41.6, eccentricity-to-column width ratios of 0, 0.2, 0.5, and 1 and reinforcement ratios of 0.9, 1.34, and 2.55% were tested. It was observed that concrete crushing was the only failure mode with very little post-peak deformation and

without any FRP rupture in tension. Khorramian and Sadeghian (2019a) developed an analytical-numerical method verified by test data and conducted a preliminary study on the behavior of slender concrete columns, but no experimental study on slender columns was conducted. Recently, Elmessalami et al. (2019) reported that a total of 129 and 100 short FRP-RC column have been tested under concentric and eccentric loading, respectively. However, only 29 slender FRP-RC columns have been tested. Very recently, Abdelazim et al. (2020) performed 20 more experimental tests on circular GFRP RC columns with slenderness ratios of 14, 19, 23, 26, and 33, and eccentricity-to-diameter ratios of 0, 0.16, 0.33, and 0.66 to expand the database. They also developed a second order model for slender RC columns and indicated that the slenderness limit of 18 is appropriate for GFRP RC columns. The statistics shows that there is a lack of test data on the behavior of slender FRP-RC columns and more experimental tests are required, which was the motivation of the current study.

The other motivation of the current study was evaluating the behavior of GFRP bars in compression and their ability to accommodate large deformations of slender columns. Many of the experimental tests were stopped once the concrete spalling happened during the tests (Khorramian and Sadeghian, 2017b; Afifi et al., 2014; Tobbi et al., 2014; De Luca et al., 2010), which does not consider the potential of the FRP-RC columns to bear loads after concrete spalling. If bars in compression are effective in the system, due to their high strength and linearity of stress-strain curves, as the deformation and strain of concrete increase, the column could still sustain loads even after concrete spalled. However, to examine this idea experimental evidence is required. It is believed that compression bars are not effective in compression and their contribution has been neglected in the design. It should be noted that the contribution of GFRP bars in compression is neglected by ACI 440.1R-15 (2015) and other design codes such as CSA S806-12 (2017), CSA

S6-14 (2014), and FIB Bulletin 40-07 (2007). This assumption underestimates the capacity of short GFRP-RC columns (Tobbi et al., 2012, Khorramian and Sadeghian, 2017a). GFRP bars showed to contribute 10% of the column capacity which was close to 12% contribution of steel bars according to the results of concentrically loaded GFRP-RC columns by Tobbi et al. (2012). Another study by Fillmore and Sadeghian (2018) indicated that the contribution is proportional to the reinforcement ratio of GFRP bars in concrete columns under pure compression. Hence, the contribution of GFRP bars ranged from 4.5% to 18.4% as the reinforcement ratio varied from 1.6% to 5.7%. Moreover, Khorramian and Sadeghian (2017a) performed a parametric analysis on short GFRP-RC columns and observed that the gain in the capacity of the columns at peak load varied from 2% to 10% for axial capacity and from 4% to 11% for flexural capacity when the eccentricity-to-column width ratio varied from 5% to 100%. However, at the design strain of 0.003 mm/mm for concrete in compression per ACI 318-19 (2019), only a maximum of 2% and 4% gain in axial and flexural capacities were observed by considering GFRP bars in compression at 5% eccentricity-to-column width ratio, which tends to lower values at higher eccentricities. It should be noted that recently, the design strain of 0.002 mm/mm for FRP bars in compression is allowed per CSA S6-19 (2019).

In terms of flexural stiffness, Zadeh and Nanni (2017) conducted a study on the flexural stiffness of FRP-RC columns in concrete frames and proposed an equation for flexural stiffness used in the moment magnification method for considering second-order effects in which the compression bars were neglected in the derivation of the suggested equations. However, neglecting the effect of GFRP bars in compression, may underestimate the flexural stiffness of slender columns. Therefore, in this research, the experimental behavior of slender GFRP-RC columns under eccentric compression is investigated to evaluate the performance of GFRP bars in

compression and under large lateral deformations due to secondary moments induced by effect of slenderness. In addition, the performance of available equations for estimating the flexural stiffness of the columns was examined to be used in the moment magnification method for design of slender GFRP-RC columns.

EXPERIMENTAL PROGRAM

Test Matrix

A total of ten GFRP-RC columns with a rectangular cross-section of 205 × 306 mm were prepared and tested under eccentric axial compression loading. The dimensions of the cross-section were selected based on the capacity of the testing equipment. As presented in Table 1, nine of the columns were reinforced with #6 GFRP bars. One specimen was reinforced with six 10M steel rebars as control specimen. As shown in Fig. 1, four U-shape #3 GFRP bars with a cross-sectional area of 71 mm^2 were tied inside each other to form two closed rectangular ties with an outer radius of 63.5 mm at the corners. The concrete cover provided for the specimens was 25.4 mm from the outer surface of the GFRP ties to the formwork. Moreover, the corners of the specimens were chamfered with a straight leg of 40 mm to prevent sharp corners.

The experimental variables were slenderness ratio and reinforcement ratio. Four different specimen lengths of 1020, 1320, 2440, and 3660 mm were prepared, corresponding to slenderness ratios ($\lambda=kl/r$) of 16.6, 21.5, 39.7, and 59.5, respectively. Slenderness ratio of 17 was proposed by Mirmiran et al. (2001) as the critical slenderness ratio for GFRP-RC columns while ACI 318-19 (ACI 2019) suggested a critical slenderness ratio of 22 for unbraced conventional steel-RC columns, and most recently a slenderness limit of 18 was introduced by Abdelazim et al. (2020b). A range of 25 to 33 is a very common slenderness ratio for residential buildings. However, higher range of slenderness ratios can be applicable for commercial buildings and bridge piers. Therefore,

the slenderness ratio of 39.7 was the core of the current study and to further observe the effect of slenderness, the slenderness ratio of 59.5 was selected. Three reinforcement ratios were considered as 4.80, 2.87, and 1.00 % which were corresponding to 10 GFRP bars, 6 GFRP bars, and 6 steel bars, respectively. For the sake of comparison, 10#6 GFRP bars were considered to provide a similar axial stiffness to the control column. Also, to compare the effect of reinforcement ratio, 6#6 GFRP bars were considered as the second reinforcement ratio at almost half of the first one. The bar layout for specimens reinforced with 10 GFRP bars, 6 GFRP bars, and 6 steel rebar are presented in Fig. 1(a), (b), and (c), respectively.

As presented in Table 1, the general form of specimen ID is "(A)(a)-e(b)-r(c)-N(d)", where the first letter (A) introduces the type of reinforcing bar, G for GFRP and S for steel, the letters (a), (b), (c), and (d) represent the slenderness ratio, eccentricity-to-column width, reinforcement ratio, and the test number at certain slenderness ratio, respectively. For example, a specimen ID of "G40-e21-r2-N3" represents a GFRP-RC column with a slenderness ratio of 39.7, eccentricity-to-column width of 0.21, reinforcement ratio of 2.87 %, and it shows that it was the third test at that eccentricity ratio.

The center to center spacing of GFRP ties was 150 mm throughout the column to prevent longitudinal bars from buckling, especially after concrete spalling. The minimum spacing of the ties was determined by the least of three according to Nanni et al. (2014): least dimension of the column (205 mm); twelve times longitudinal bar diameter (228 mm); twenty-four times tie bar diameter (240 mm). It was determined by Paultre and Légeron (2008) and confirmed later for GFRP ties by Maranan et al. (2016) that the effect of confining reinforcement in restraining concrete is negligible when the ties are spaced more than half of the minimum core cross-section dimension. Moreover, Guérin et al. (2018a) studied eccentric behavior of GFRP-RC columns using

bars and ties which confirmed the findings regarding confinement for eccentric loading. As the current study was not designed to account for the confinement effect, 150 mm was selected for spacing in order to minimize the confining effect, which is lower than the minimum (205 mm) and higher than half of the core cross-section dimension. To provide the same confinement level for all specimens, even the steel RC column was reinforced with transverse GFRP ties. Previously, Hales et al. (2016) used longitudinal steel reinforcement and GFRP spirals to maximize the confined core area by reducing the cover made possible by a non-corrosion characteristic of GFRPs. To prevent a possible premature failure at the ends of columns at a distance twice the depth of column, the spacing of the ties reduced to 75 mm.

Material Properties

The summary of the material properties, which are the average ± standard deviation of the performed tests except for bar #3, are presented in Table 2. To determine the tensile characteristics of longitudinal GFRP bars, with a nominal diameter of 19 mm and a nominal area of 285 mm^2, five tensile GFRP coupons were built and tested per ASTM D7205M-16 (ASTM 2016). It should be noted that for the calculation of the tensile strength and modulus of the GFRP bars, the nominal cross-section of the bars was used. However, according to the immersion test performed on 5 coupons for #6 and #3, the cross-sections were determined as 314 mm^2 and 86 mm^2, respectively (with a variation range of ±9 mm^2). Fig. 2 shows a photograph of the bars used in the research along with a ruler. The compressive properties of #6 GFRP bars were also determined by testing five compressive coupons based on the test method proposed by Khorramian and Sadeghian (2019b and 2018) and presented in Table 2. The modulus of elasticity of the GFRP bars in both tension and compression was found using the strain vales between 0.001 and 0.003 mm/mm. It should be noted that the compressive modulus of elasticity is 13% higher than the tensile modulus

of elasticity for longitudinal bars which is compatible with the findings of experimental tests performed by Khorramian and Sadeghian (2019b). The ties were built using #3 GFRP bars with a nominal diameter and cross-sectional area of 10 mm and 71.26 mm^2, respectively. The properties of the ties were provided by the GFRP bar manufacturer (Owens Corning, Toledo, OH) as presented in Table 2.

The concrete was ready-mix with a maximum aggregate size of 12 mm and a slump of 200 mm. The 28-day concrete strength was determined as 48.4 ± 0.7 MPa by testing three 100×200 mm concrete cylinders per ASTM C39M-18 (ASTM 2018), and at the time of testing five concrete cylinders (150×300 mm) were tested and the results are presented in Table 2. It should be mentioned that all columns were cast from the same concrete batch. Moreover, five tensile coupons of the steel rebars were prepared and tested per ASTM A370M-18 (ASTM 2018). It should be noted that in order to calculate the tensile strength and modulus of elasticity of steel bars, the nominal cross-section (100 mm^2) minus two machined areas for strain gauging with a width of 6 mm and depth of 1 mm was considered which gives a cross section of 88 mm^2.

Test Setup and Instrumentation

The concrete columns were tested under eccentric axial compression loading using the test setup presented in Fig. 3. The test fixture includes two concrete end blocks, a swivel, a 2 MN actuator, a spherical platen, a load cell, a tunnel, a shaft, two sets of steel caps, two sets of steel belt, three sets of steel rollers. A V-notched welded plate was put at the center of the steel roller installed on the shaft and end block which provides the simply supported boundary condition for each end of the columns, as shown in Fig. 3. The distance between the center of the V-notched plate and the center of the specimen gave the desired load eccentricity. Moreover, two different load eccentricities of 42.5 and 47.5 mm were selected which were corresponding to 21 and 23 % of the

width of column cross-section (205 mm). It should be mentioned that the eccentricity is applied on the width of the column cross-section (205 mm) because it provides a lower lever arm for bars and the testing machine can reach the column capacity. Fig. 4(a) shows the steel test fixture that holds the end of the specimen. Two V-notched steel plates were welded to the end of the steel plate as shown in Fig. 4. The target eccentricities were 40 and 50 mm. However, later 2.5 mm shift occurred in the eccentricity in the welding of the test fixture which made 42.5 mm and 47.5 mm as the actual load eccentricities as shown in Fig. 4. It should be noted that since these two eccentricities are close to each other, the eccentricity was not considered as a test parameter. To increase the integrity of the column and steel cap setting, two grout bags were put between steel cap and concrete columns at both ends. Also, both ends of all specimens were strengthened by applying three layers of GFRP wrapping in a total length of 200 mm, to prevent possible premature failure at the ends of the specimens. Since the tests were performed horizontally, three sets of steel rollers were installed at the bottom of the concrete specimens as shown in Fig. 3.

The data acquisition system included linear potentiometers (LPs), string potentiometer (SPs), strain gauges (SGs) as presented in Fig. 3. It should be noted that the load and stroke position were also recorded both by the controller and the data acquisition system. The lateral displacement of the concrete columns was recorded at the middle height of the columns using four LPs. Two of the LPs were installed at the midsection in compression and tension sides as shown in Fig. 3. On top of the specimen and at the centerline of the specimens, an angle-shaped aluminum profile with a length of 50 mm was bonded to the specimen using adhesives. For short columns, two more LPs were installed to capture the lateral displacement from to aluminum angle. However, for slender columns, due to the existence of larger lateral displacements, two SPs were used to obtain the lateral displacement of the column at the center of the aluminum angle as shown in Fig. 3. To

record the strain of the GFRP bars, eight strain gauges were used. The stains were recorded at three different sections through the length of the column; at midsection (section A-A) and at two sections that were 150 mm away from the mid-height of the columns (section B-B). The strains of the middle bars in tension and compression were recorded in all mentioned sections as shown in Fig. 3. In addition, the tensile and compression strain of the corner bars were recorded in the middle section. The tests were performed by using a displacement control approach with an axial displacement (stroke) rate of 2 mm/min. Moreover, the data was recorded with a rate of 10 data per second.

EXPERIMENTAL RESULTS AND DISCUSSION

Table 3 presents the summary of the test results including the peak load (P_u) and the axial displacement (Δ_{axial}), lateral displacement ($\Delta_{lateral}$), and bending moment (M_u) corresponding to the peak. It should be noted that specimen G17-e23-r4-N1 was tested three times and had experienced premature failure at the end of the specimen twice. The latter happened because the steel cap was not tight enough to make the specimen rotate at the ends. Each time, the end of the specimen was strengthened with grout and wrapped with GFRP wrapping before retesting. This was at the early stages of the testing, and later the issue was fixed by using steel belts to tighten the steel caps at the ends as discussed in the previous section. Therefore, this specimen will not be considered in the rest of the study.

By comparing the results presented in Table 3, it is observed that some of the results were not as expected (i.e. G40-e23-r4-N2 and G22-e23-r4-N1). For example, a column with a higher slenderness ratio (i.e. G22-e23-r4-N1) sustained more load than the specimen with a lower slenderness ratio (i.e. G17-e23-r4-N2), which was not expected. Therefore, further investigation

showed that the location of the bars was not the same for all specimens, as presented in Table 3. After testing, the specimens were cut perpendicular to their longitudinal axis to find out a more accurate location of the longitudinal bars in the cross-section. The columns were cut after they were tested, when the concrete in the middle section was crushed. Therefore, the cut sections located at a section 306 mm far from the end of the columns. It was observed that the bars were not at the same location since the location of the bars was dictated by the large corner radius of four U-shape stirrups. All longitudinal bars were straight along the length of the column and were supported by ties in the plane of flexure as shown in Fig. 5(a). Four U-shape ties completely supported each bar but caused bar locations not to be in a line in the section as presented in Fig. 5(b). The GFRP stirrups are not bend-able like steel ones, therefore, the difference in the bar locations is unavoidable, and the situation is representative of real practice. The latter is a practical issue due to large radius of FRP ties in comparison to steel ties which causes different bar locations in the section, and as the number of tie corners increases, the bars are more prone to be locate in different heights with respect to the edge of the concrete. After the section was cut, the location of the center of each bar was measured from the furthest compression fiber. The centroid of GFRP bars in the compression side (d_1) and in the tension side (d_2) were measured from the furthest compression fiber in concrete and presented in Table 3 and Fig. 5(b). Other sources of error were the inaccuracy in the eccentricity that varied as much as ±3 mm (due to the existence of the grout bags between concrete and steel caps), and the variability in the size of chamfers (±2 mm for the legs of chamfers), and variability in the dimension of the columns (±1 mm for width of columns). The behavior and results are discussed in more detail in the following sections. Per ACI 318-19 (ACI, 2019), in steel-RC columns, every corner and alternate longitudinal bar shall have the lateral support provided by the corner of a tie. No unsupported bar shall be farther than 150 mm clear on

each side along the tie from a laterally supported bar. The bar arrangement in this study satisfies the requirement. It should be highlighted that the requirement is the process of being adopted by the in-progress ACI code for GFRP-RC columns.

Failure Modes

In the current study, a total of three modes of failure were observed including concrete spalling/ crushing (CC), global buckling (GB), and GFRP crushing (GC), as presented in Fig. 6. It should be highlighted that no GFRP crushing was observed prior to concrete failure. No rupture of tensile GFRP bars occurred during the tests. Fig. 7(a) and Fig. 7(b) present axial load-axial displacement curves of the slender concrete columns. It is seen that the unloading part was captured for slender columns. The loading stages are shown in Fig. 8. For short columns, the specimens did not experience buckling and the peak load was almost corresponding to the spalling/crushing of the concrete. A very slight drop after peak load was observed. For slender columns, the columns buckled first, and concrete crushing happened afterward as shown in Fig. 8. After concrete spalling/crushing, the behavior of both slender and short GFRP-RC columns followed the same pattern. A sudden drop in axial load was observed after concrete crushed as shown in Fig. 8. As the test was performed with a displacement control approach, testing was continued after load dropped. The softening trend was continued with a shallow downward slope to reach the crushing of GFRP bars in compression, as presented in Fig. 8. After the GFRP bar crushing, a sudden drop happened as the displacement increased. Therefore, the tests were stopped, and the unloading procedure started with a displacement rate of 4 mm/min to capture the unloading part as presented in Fig. 8. It was observed that as the displacement decreases in the unloading branch, the specimens became straight and the axial load-axial displacement curves tend to come back to the origin indicating the resiliency of the GFRP-RC columns, as shown in Fig. 7.

The additional ability to sustain loads after concrete spalling/crushing can be attributed to the elastic behavior of GFRP bars and their high strength in compression. Such behavior was not observed in the steel-RC specimen. Instead, after concrete crushed, the deformation was not reversible like the GFRP-RC specimens. It should be noted that there was not enough steel reinforcement in the control specimen to see ductile behavior as a minimum reinforcement ratio of 1% was considered. However, even if the steel reinforcement ratio was sufficient, at large deformations, many layers of reinforcements would be yielded and then the column would experience a permanent displacement, due to permanent plastic deformations after steel yielding, which is different than the observations for GFRP-RC columns with high resiliency. The axial stiffness of steel-RC column and GFRP-RC column at slenderness ratio of 22 (which is known as the critical slenderness ratio for the steel-RC columns in unbraced frames) was kept the same, which lead to almost the same axial capacity of the column. It was observed that, before failure, the steel-RC column experienced more lateral deformation and hence more moment capacity in comparison with the GFRP-RC column. However, there was no additional capacity after concrete crushed in the steel-RC column.

Load-Displacement Behavior

The axial load-lateral displacement curves for short and slender columns are presented in Fig. 9(a) and Fig. 9(b), respectively. It is seen that for all GFRP-RC specimens, there was a sudden jump in the lateral displacement after concrete crushed at the midspan. However, the specimens continued to experience more lateral displacement up to the crushing of GFRP bars in compression. It should be noted that the slenderest column (i.e. G60-e23-r4-N1) did not experience GFRP bar crushing since the test was stopped due to safety concerns in the lab. For G60-e23-r4-N1, a considerable lateral displacement at the midspan was observed (i.e. 193.7 mm) and the rotational capacity of

the test fixture at the ends of the columns was very considerable before the test was stopped. It was observed that specimens with higher slenderness ratio experiences more lateral deformation. Table 4 presents the displacement values corresponding to concrete spalling/crushing and crushing of GFRP bars or termination of the test. On average, specimens experienced 61.2 mm additional displacement after concrete crushing which is almost three times more than the displacement at the concrete crushing/spalling point. The ability of columns to sustain extra load and displacement after the peak provides larger area under the load-displacement response of the column, which means extra energy is required to cause total failure of each member. The latter can be used to perform further studies on a system of columns which benefits the post peak behavior to capture the full capacity of the system, which requires an independent study and is out of scope of the current study.

To examine a potential benefit of this behavior, consider a system of beams and columns built with GFRP-RC members. The post peak behavior can be used for establishing a new definition of failure for GFRP-RC columns as the crushing point of GFRP bars in compression instead of spalling of concrete at peak load. Then, by allowing post peak behavior to be considered in the analysis of a system of columns, one column may fail after the other to finally cause the total failure of a system of columns. This progressive failure of the system can be modeled to give the response of the system which uses the capacity of all members. By analyzing the same system and considering only the elastic response of the system up to peak load. By comparing the response of the elastic system against the system with progressive failure, a new performance-based design procedures can be established based on the full load-deflection behavior of the columns instead of using only the capacity of the columns at the peak load. Then, reliability-based analysis will be required to determine the safety of the system based on the full load-deflection behavior of the

columns. Although the post-peak behavior observation in this study may assist building new models for such analysis, the establishment of the design procedure for the explained system is out of scope of this paper.

Loading Path Behavior

By multiplying the axial load (P) by the sum of lateral displacement (Δ) and initial eccentricity (e_0), at each loading step, the corresponding bending moment ($M = P\times(e_0+\Delta)$) can be calculated. Plotting the axial load versus the bending moment creates a curve known as loading path. The loading path for short and slender column specimens is presented in Fig. 10(a) and Fig. 10(b), respectively. After concrete crushed and a sudden drop in load happened, there was an additional moment resistance in the specimens. Table 4 shows that, on average, the moment capacity is dropped only 9% after concrete crushed up to the crushing of GFRP bars in compression. Therefore, the ability of the column to sustain more lateral displacement leads to similar moment capacities at concrete spalling/crushing and after that up to GFRP bar crushing.

By using the data presented in Table 3 for the values of peak load, and Table 4 for the values of the load when concrete crushed, the drop of the load before crushing can be determined. The average drop in load from peak load to the crushing point was 0.62% for short GFRP_RC specimens, 1.00% for the specimens with a slenderness ratio of 39.7, 15.60% for the specimen with a slenderness ratio of 59.5, and 4.79% for the steel-RC specimen. The tests showed that, for the slenderness ratio of 22, the average drop of the load after peak load up to concrete spalling for GFRP-RC columns (i.e. 0.46%) was more than ten times smaller than the drop for the steel-RC specimen (i.e. 4.79%). The latter shows that the slenderness effect was less for GFRP-RC columns than for steel-RC columns. The average load drop from concrete spalling/crushing to crushing of GFRP bars in compression was 48.5% as presented in Table 4.

Strain of GFRP Bars in Compression

In terms of strain records, since the location of the GFRP bars was different in the section as shown in Table 3, the strain of GFRP bars even at the same section was different. It is seen that short specimens reached higher compressive strain when concrete crushed. On average, GFRP bars in compression experienced 63% and 36% more strain in comparison with the slender specimens. The latter justifies that the slender GFRP-RC columns were able to sustain more than four times extra lateral displacement in comparison with the short columns. Thus, the slender GFRP-RC columns can provide more deformability and reach higher strains at much larger lateral displacements than the short columns. The load-strain profiles for the columns are presented in Fig. 11.

Table 5 presents the compressive strain of the GFRP bars at the mid-section of the columns. To secure the values recorded by strain gauges installed on bars in compression, special consideration for preparation was considered to avoid crack of matrix and local buckling of fibers and have proper strain gauge recording (Khorramian and Sadeghian, 2019b). The average strain of GFRP bars in compression at the peak load was 0.0024 mm/mm which is only 17% of their expected crushing strain found in the material tests (0.014 mm/mm). It should be noted that in some cases, the strains at the final stage (GC) were not available. Therefore, for those cases, the maximum strain recorded was selected which was less than the actual strain at the end of the loading stage. It was observed that, on average, the additional stains that GFRP bars experienced after concrete crushed were 0.0070 mm/mm and 0.0099 mm/mm for the compression side and tensile sides, respectively. This justifies the extra moment capacity of the specimens after concrete crushed and explains the mechanism of failure (presented later in the contribution of the GFRP

bars section). The failure of concrete led to a decrease in the resultant concrete compressive force in section, which suddenly led to a drop in axial and moment capacity. However, due to the presence of the compressive GFRP bars, after a drop, equilibrium was satisfied in the section. As the result, as the loading continued after the concrete spalling/crushing stage, the strain in both compressive and tensile sides increased and the compressive force in GFRP bars increased. The action contributed more in bending capacity of the columns up to the crushing of GFRP bars in compression after the peak load. The GFRP bars were started to buckle once the concrete spalled which lowered down the lateral support of longitudinal bars and caused local buckling of bars before GFRP bars reached their compressive crushing strain obtained from material tests. The average compressive strain of GFRP bars at the ultimate stage (GC) was 0.0102 mm/mm which was 73% of the average crushing strain found by material testing (0.01399 mm/mm). Since the slenderest specimen did not experience crushing of GFRP bars, it was excluded from this average. Therefore, overall, the compressive GFRP bars were very effective especially in creating deformability and keeping the section in equilibrium after concrete spalling/crushing.

Moment-Curvature Behavior

The moment-curvature curves of the specimens at mid-height are presented in Fig. 12. The moments and curvatures were determined from strain profiles at each load step. The strain profile was derived by fitting a straight line to the values of strain gauge records at the mid-height section. The strains at each section for each strain gauge can be found in Fig. 11. As shown in Fig. 12, it is observed that for all GFRP reinforced concrete specimens, the moment-curvatures curves showed a secondary hardening branch after failure of columns at the peak load due to concrete crushing/spalling. In other words, it was observed that after GFRP-RC specimens reached their capacity, the equilibrium was satisfied, and the specimens were able to sustain loads to gain extra

moment capacity after the drop in the peak load. The latter can be attributed to the effect of GFRP bars in compression. After concrete spalling/crushing, the equilibrium is disturbed and while the lateral deformation increases, the moment decreases due to a sudden drop in the axial load capacity. Meanwhile, the curvature of the crushed column increases which causes an increase in the strains of compressive GFRP bars. Thus, although concrete is able to sustain less compressive loads, compressive GFRP bars start to contribute more considerably in the compressive side. It should be noted that the ties did not fail during the test, and ties acted as lateral support for the longitudinal GFRP bars. As the contribution of GFRP bars in compression increases due to an increase in the curvature, the bending moment increases up to the moment that GFRP reaches its crushing in compression or buckles. This mechanism is attributed to the linear stress-strain relationship of FRPs which makes them gaining strength even after concrete failure. It should be mentioned that in a recent study on the moment-curvature behavior of GFRP-RC columns, Hasan et al. (2019) observed similar moment-curvature behavior using analytical-numerical methods.

Flexural Stiffness

To further investigate the behavior of the specimens, their flexural stiffness was obtained from the moment-curvature curves. Fig. 13 shows four different points on the moment-curvature curves that represent different flexural stiffnesses corresponding to peak load (EI_{Peak}), concrete spalling (EI_{SP}), the design strain of 0.003 mm/mm at the furthest compression fiber in compression (EI_{D}), and the strain corresponding to GFRP crushing (EI_{GC}). The flexural stiffnesses obtained from the experimental data can be compared to the formulas for the estimation of the flexural stiffness available in the literature as presented in Eq. 1 to Eq. 10. Table 6 presents the formulas available in the literature (Eqs. 1-10) for the prediction of the flexural stiffness of the concrete columns used in the moment magnification method to account for the slenderness effects. It should be mentioned

that a high presumed eccentricity is embedded in Eq. 1, Eq. 2, Eq. 7, and Eq. 9, since the equations meant to be used for design purposes where the eccentricity values are not known in advance.

$$EI_1 = 0.4E_cI_g \tag{1}$$

$$EI_2 = 0.2E_cI_g + E_sI_s \tag{2}$$

$$EI_3 = E_cI;\ 0.35I_g \le I = \left(0.80 + 25\frac{A_{st}}{A_g}\right)\left(1 - \frac{M_{ult}}{P_{ult}h} - 0.5\frac{P_{ult}}{P_o}\right)I_g \le 0.875I_g \tag{3}$$

$$EI_4 = \frac{0.7}{0.75} \times [(0.27 + 0.003\,l/h - 0.3\,e/h)E_cI_g + E_sI_s] \tag{4}$$

$$EI_5 = \frac{0.7}{0.75} \times [(0.3 - 0.3\,e/h)E_cI_g + E_sI_s] \tag{5}$$

$$EI_6 = \frac{(0.36 + 0.05\mathrm{n} - 0.3\mathrm{e/h})}{0.75} \times (0.2E_cI_g + E_fI_f) \tag{6}$$

$$EI_7 = \frac{(0.2 + 0.06\mathrm{n})}{0.75} \times (0.2E_cI_g + E_fI_f) \tag{7}$$

$$EI_8 = E_cI;\ I = \left(0.80 + 25\frac{A_f}{A_g}\frac{E_f}{E_s}\right)\left(1 - \frac{M_{ult}}{P_{ult}h} - 0.5\frac{P_{ult}}{P_o}\right)I_g \le 0.875I_g \tag{8}$$

$$EI_9 = 0.2E_cI_g + 0.75E_fI_f \tag{9}$$

$$EI_{10} = \frac{0.7}{0.75} \times \left(\left[0.45 - \left(1 + 0.01\frac{l}{h}\right)\left(\frac{e}{h}\right) + 0.008\frac{l}{h}\right]E_cI_g + E_fI_f\right) \tag{10}$$

For consistency in the calculations, all formulas were normalized to have the same stiffness reduction factor of 0.75. It should be noted that for the calculation of the flexural stiffness, the effect of chamfers was deducted from the concrete section, and the values of d_1 and d_2 (see Table 3) were used to calculate the effect of reinforcing bars in the calculations. Moreover, the modulus of elasticity of concrete was calculated based on the equation (i.e. $E_c = 4700\sqrt{f_c'}$) by ACI 318-19 (2019). Also, the nominal cross-sectional area of bars was considered, and the modulus of elasticity of steel and FRP were considered as 200 GPa and 43.4 GPa, respectively, as reported by the manufacturer. To calculate P_{ult} and M_{ult}, which are the ultimate factored loads, $0.65P_D$ and $0.65M_D$ were considered with a reduction factor of 0.65 per ACI 440.1R-15 (2015) for calculation of

ultimate factored loads. It should be noted that the values of P_D and M_D are presented in Table 8. The value of P_o was calculated based on Eq. 11 (ACI 318-19, 2019) in which f_y was replaced by the modulus of elasticity of GFRP bars times the design strain of 0.002 mm/mm per CSA S6-19 (2019), and A_{st} was replaced by A_f for GFRP RC columns. All parameters are described in the list of notations.

$$P_o = 0.85f'_c\left(A_g - A_{st}\right) + f_y A_{st} \quad (11)$$

The results for the flexural stiffness calculated with different formulas presented in Table 6 are presented in Table 7 along with the ones obtained from the experimental program. Moreover, Fig. 14 presents a comparison of the *EI* equations from literature with the design flexural stiffness calculated based on the experimental tests at the strain of 0.003 mm/mm at the furthest compression fiber in concrete. The results showed that most of the current equations underestimated the flexural stiffness. Eq. 10 gives the closest value to the experimental design flexural stiffness corresponding to the strain of 0.003 mm/mm at the furthest compression fiber in concrete.

Eq. 4 and Eq. 5 are giving the best estimation of the flexural stiffness at concrete spalling. It was observed that Eq. 1, Eq. 3, and Eq. 8 overestimates the flexural stiffness, and for most cases, the upper limit of $0.875E_cI_g$ was controlling Eq. 3 and Eq.8. Also, the results showed that flexural stiffnesses which were calculated by Eq. 6 and Eq. 7 are considerably underestimating the experimental values. Therefore, beside these equations, Eq. 2 and Eq. 9 are the most conservative equations for estimation of the flexural stiffness. Since Eq. 9 was derived based on neglecting GFRP bars in compression from Eq. 2, it gave lower stiffness values than Eq. 2. However, the stiffness values calculated by Eq. 2 are closer than Eq. 9 to the experimental values at the design level. Thus, the comparison shows that the equation which considered the contribution of GFRP

bars in compression (i.e. Eq. 9) is more realistic and accurate than the one ignoring the contribution of GFRP bars in compression (i.e. Eq. 2). It should be noted that this conclusion is valid for the range of tested eccentricity.

Moment Magnification Factor

The equations for moment magnification factor (δ) per ACI 318-19 (ACI 2019) are presented in the following:

$$P_{cr} = \frac{\pi^2 EI}{(kl)^2} \tag{12}$$

$$\delta = \frac{C_m}{1 - \frac{P_{ult}}{0.75P_{cr}}} \tag{13}$$

All parameters are described in the list of notations. Table 8 presents experimental and calculated moment magnification factors at design loads and at peak loads. In the calculation, C_m was considered as 1 since the columns were tested under pin-pin boundary condition. To calculate P_{ult}, which is the ultimate factored load, $0.65P_D$ and $0.65Pu$ were considered to calculate moment magnification factors corresponding to EI_D and EI_u, respectively. It should be noted that to reflect the effect of the factored loads, a reduction factor of 0.65 was considered for columns per ACI 440.1R-15 (2015) and ACI 318-19 (2019). For calculation of the experimental ratios, the moments at design and peak loads to their corresponding first-order moments (initial eccentricity times load), were considered as the experimental moment magnification factors. The results showed that the ratio of the calculated to experimental moment magnification factors at design loads and peak load are 0.95 and 0.94, respectively. The outcome shows that, for the range of tested specimens, the calculated moment magnification factor is less than the experimental values which is unconservative. Thus, further investigations are required to refine the equations for calculation of the moment magnification factors for GFRP-RC columns.

Contribution of GFRP Bars in Compression

The procedure to determine the contribution of compressive GFRP bars in axial and moment capacities is illustrated in Fig. 15(a). In order not to overestimate the effect of bars, the minimum recorded strain (of all strain gauges installed on FRP bars in column tests) at compression and tensile sides were used to assess the internal forces of the GFRP bars at peak load and crushing of GFRP bars using Eq. 14.

$$F_{fc} = E_{fc}\varepsilon_{fc}A_{fc};\ F_{ft} = E_{ft}\varepsilon_{ft}A_{ft};\ F_C = (P_u\ or\ P_{GC}) - F_{fc} - F_{ft} \quad (14)$$

To calculate the internal moment corresponding to GFRP bars and concrete, the curvature of the section was determined using the compressive and tensile strains of GFRP bars using Eq. 15, and from the curvature the lever arms for the internal forces in GFRP bars were found. Afterward, the moment resistance due to GFRP bars in compression, GFRP bars in tension, and concrete in compression at peak load and crushing of bars in compression were calculated using Eq. 16. The Calculated values for compressive forces and all moments are available in Table 9.

$$\psi = \frac{\varepsilon_{ft} - \varepsilon_{fc}}{d_2 - d_1} \quad (15)$$

$$M_{fc} = F_{fc}d_{fc};\ M_{ft} = F_{ft}d_{ft};\ M_C = (M_u\ or\ M_{GC}) - M_{fc} - M_{ft} \quad (16)$$

It should be noted that M_u *and* M_{GC} in Eq. 16 should be calculated by considering a lever arm from the neutral axis to the location of the axial load, since the moment equilibrium in the section was satisfied about the neutral axis for Eq. 16, as shown in Fig. 15(a). Fig. 15(b) and Fig. 15(c) show the contribution of concrete and GFRP bars in compression to resisting the sum of external compressive load and internal tensile force at peak load and at crushing of GFRP bars in compression. On average, the contribution of GFRP bars in compression and concrete in load resistance at peak load were 11% and 89%, respectively, while the contributions at crushing of GFRP bars were 44% and 56%, respectively. The results showed that the contribution of GFRP

bars in compression increases after concrete spalling and reaches 80% of concrete contribution at crushing of GFRP bars, which means GFRP bars in compression significantly contributed to carrying capacity after concrete spalled. The contribution of steel bars at peak load was 8% which is less than the contribution of GFRP bars in compression (11%) while the axial stiffness was kept the same. The latter showed that GFRP bars in compression are as effective as steel in compression up to the peak load.

Fig. 15(d) and Fig. 15(e) show the contribution of concrete, GFRP bars in compression, and GFRP bars in tension at peak load and at crushing of GFRP bars in compression. On average, the contribution of concrete, GFRP bars in compression, and GFRP bars in tension to moment resistance at peak load were 94%, 5%, and 1%, respectively, while the contributions at crushing of GFRP bars in compression were 51%, 23%, and 26%, respectively. At peak load, the contribution of concrete was superior, and the tensile contribution of the GFRP bars was almost negligible (1%). However, after concrete spalled, the contribution of GFRP bars in compression and tension increased drastically. For short columns, the concrete contribution in moment resistance was 35% in comparison to 43% contribution of GFRP bars in compression. As slenderness increased, the contribution of GFRP bars in compression in the moment resistance declined while the contribution of concrete and tensile GFRP bars increased. It should be highlighted that the effect of confinement is embedded in the contribution of the concrete and does not affect the values presented for the contribution of GFRP bars, as their contribution have been directly calculated using recorded strain values at each loading stage. However, the contribution of concrete was found by subtracting the effect of bars from the capacity of the column at each loading stage, which makes the confinement effect inside the concrete values presented for

concrete and not GFRP bars. In other words, when concrete (unconfined or confined) crushes and loses its stiffness, GFRP bars are still elastic and way below their crushing strain.

Theoretical Evaluation

This brief theoretical evaluation is provided here to evaluate the effect of eccentricity on the performance of one of the specimens tested in the experimental program, as the eccentricity-to-column width ratios of 0.21 and 0.23 in the experimental program were very close to each other. An analytical-numerical model was adopted from an earlier study by the authors (Khorramian and Sadeghian, 2017a). The model considers the nonlinearity of both material and geometry and involves an iterative procedure to find the load-strain and load-displacement curves. Fig. 16(a) and 16(b) present a comparison between the load-displacement and load-strain curves, respectively, obtained from the analytical-numerical model and three of the test specimens of the current experimental study. The model showed a very good agreement for slenderness ratios of 21.5 and 39.5, and a good agreement for slenderness ratio of 59.5. Using the model, the eccentricity-to-column width ratios of 0.05, 0.1, 0.2, 0.3, and 0.5 were considered, as presented in Fig. 17. It is observed that as eccentricity increases, the peak load decreases and the displacement corresponding to that increases. Also, it is observed that the post peak behavior for the load-displacement curves tends to be expanded and the crushing of concrete, which is corresponding to the end of the curves, occur at higher displacements. In this section, only the effect of eccentricity for a group of test specimens with 10 GFRP bars and the slenderness ratio of 39.4 was considered. The theoretical study needs to be expanded in the future to evaluate a broad range of parameters establishing a data platform for a comprehensive reliability analysis for design applications.

FUTURE STUDIES

This study showed that the crushing of GFRP bars occurred way after the peak load of the column specimens. Also, the GFRP-RC specimens were able to sustain significant amount of load after the peak load up to the crushing of GFRP bars in compression. This was attributed to the contribution of GFRP bars in compression. As the result, first, the contribution of GFRP bars in compression for the calculation of flexural stiffness and peak load should not be ignored in the design process of GFRP-RC columns. Moreover, the failure and post-peak behavior of the GFRP-RC columns can be quantified based on a cross-section analysis considering the softening behavior concrete in compression after the peak load and linear-elastic behavior of GFRP bars in tension and compression until the crushing strain of GFRP bars. The analysis can be included in a progressive failure analysis of GFRP-RC frames towards a performance-based design and considering the resiliency of GFRP-RC frames. In addition, the behavior of GFRP-RC columns after concrete spalling requires more investigations to define a proper deformability index. The experimental program showed that the behavior of the columns with slenderness ratios of 17 and 22 was not different and there were very slight secondary moment effects. Therefore, more studies are required to give a more realistic critical slenderness ratio, since the critical slenderness ratio defines the borders between short and slender columns. More investigations are also required for proposing a flexural stiffness which predicts the experimental results more accurately. Moreover, a comprehensive theoretical study is needed to study the effects of parameters beyond the ones considered in this study to establish a large data base for reliability-based analyses proposing reliable design parameters including stiffness reduction factors and critical slenderness ratios for different loading conditions.

CONCLUSION

In this paper, the behavior of short and slender GFRP-RC columns was investigated experimentally. Ten large-scale specimens with two different GFRP reinforcement ratios of 4.8% and 2.78%, and four different slenderness ratios of 16.6, 21.5, 39.7, and 59.5 were tested up to their ultimate failure. The following conclusions can be drawn:

- A total of three modes of failure including concrete spalling/crushing, global buckling, and GFRP bars crushing were observed. The short specimens (i.e. specimens with a slenderness ratio of less than or equal 22) did not experience global buckling. For slender specimens, the global buckling happened and followed by the concrete spalling/crushing. No GFRP crushing occurred prior to the spalling/crushing, which was corresponding to a peak load. No rupture of GFRP bars in tension observed in the tests.
- As, the loading continued after The peak load, it was observed that the GFRP-RC columns were able to sustain almost a constant load after spalling/crushing of concrete up to the crushing of the GFRP bars in compression way after the peak load. The specimens were able to tolerate lateral displacement at a certain load level which led to an increase in the moment capacity of the specimens beyond concrete crushing/spalling. This moment capacity was attributed to the compressive GFRP bars which were contributed to the axial and bending capacity especially after concrete spalling/crushing. Linear stress-strain behavior of GFRP bars and constant increase in curvature, and in turn strains, made the contribution of GFRP bars in compression more effective.
- The average compressive strain of GFRP bars in compression was 0.0102 mm/mm at the ultimate loading stage (i.e. GFRP bar crushing) which was 73% of the average crushing strain found by material compressive testing. The buckling of GFRP bars after concrete

spalling/crushing was the reason for not reaching the ultimate crushing strain for GFRP bars in compression. Crushing of GFRP bars in compression was corresponding to a total drop in the load capacity for the tested specimens which led to stop the tests.

- The unloading stage after failure showed that the bent specimens became straight and their load -axial displacement curve approaches the origin. The phenomenon indicated the resiliency of GFRP-RC columns and can be considered for development of performance-based design procedures in the future.
- The flexural stiffness of the specimens calculated from the experimental study and the ones calculated from the available formulas of the literature were compared. Many of the formulas were overestimating or underestimating the flexural stiffness.
- Overall, the contribution of GFRP bars after failure is considerable. Moreover, GFRP bars in compression were as effective as steel bars in providing the axial force and moment resistance at peak load. Also, by considering compressive GFRP bars in the calculations of flexural stiffness, more accurate results can be obtained. Therefore, it is suggested not to neglect the effect of GFRP bars in compression.

ACKNOWLEDGMENT

Authors would like to thank Jordan Maerz, Blair Nickerson, Brian Kennedy, Jesse Keane, and Brian Liekens and for their assistance in the lab. The authors would also like to acknowledge and thank NSERC and Dalhousie University for their financial support as well as Owens Corning (Toledo, OH) for providing GFRP bars.

DATA AVAILABILITY STATEMENT

Some or all data, models, or code generated or used during the study are available from the corresponding author by request (including test data).

REFERENCES

Abdelazim, W., Mohamed, H. M., and Benmokrane, B. (2020a). "Inelastic Second-Order Analysis for Slender GFRP-Reinforced Concrete Columns: Experimental Investigations and Theoretical Study." *Journal of Composites for Construction*, 24(3), 04020016.

Abdelazim, W., Mohamed, H. M., Afifi, M. Z., and Benmokrane, B. (2020b). "Proposed Slenderness Limit for Glass Fiber-Reinforced Polymer-Reinforced Concrete Columns Based on Experiments and Buckling Analysis." *ACI Structural Journal*, 117(1), 241-254.

ACI (American Concrete Institute). (2015). "Guide for the Design and Construction of Structural Concrete Reinforced Fiber-Reinforced Polymer (FRP) Bars." ACI 440.1R-15, Farmington Hills, MI, USA.

ACI (American Concrete Institute). (2019). "Building Code Requirements for Structural Concrete." ACI 318-19, Farmington Hills, MI, USA.

Afifi, M. Z., Mohamed, H. M., and Benmokrane, B. (2014a). "Axial Capacity of Circular Concrete Columns Reinforced with GFRP Bars and Spirals." *Journal of Composites for Construction, ASCE, 18*(1), 04013017.

Afifi, M. Z., Mohamed, H. M., and Benmokrane, B. (2014b). "Strength and axial behavior of circular concrete columns reinforced with CFRP bars and spirals." *Journal of Composites for Construction, 18*(2), 04013035.

AlAjarmeh, O. S., Manalo, A. C., Benmokrane, B., Karunasena, W., Ferdous, W., and Mendis, P., (2020a). "A New Design-Oriented Model of Glass Fiber-Reinforced Polymer-Reinforced Hollow Concrete Columns." *ACI Structural Journal*, 117(2), 141-156.Alajarmeh, O. S., Manalo, A. C., Benmokrane, B., Karunasena, W., and Mendis, P. (2019a). "Axial performance of hollow concrete columns reinforced with GFRP composite bars with different reinforcement ratios." *Composite Structures, 213*, 153-164.

AlAjarmeh, O. S., Manalo, A. C., Benmokrane, B., Karunasena, W., and Mendis, P. (2020b). "Effect of spiral spacing and concrete strength on behavior of GFRP-reinforced hollow concrete columns." *Journal of Composites for Construction*, 24(1), 04019054.

Alajarmeh, O. S., Manalo, A. C., Benmokrane, B., Karunasena, W., Mendis, P., and Nguyen, K. T. (2019b). "Compressive behavior of axially loaded circular hollow concrete columns reinforced with GFRP bars and spirals." *Construction and Building Materials, 194*, 12-23.ASTM (American Society for Testing and Materials). (2016). "Standard Test Method for Tensile Properties of Fiber Reinforced Polymer Matrix Composite Bars." ASTM D7205/D7205M-06, West Conshohocken, PA, USA.

ASTM (American Society for Testing and Materials). (2018). "Standard Test Method for Compressive Strength of Cylindrical Concrete Specimens." ASTM C39/C39M-18, West Conshohocken, PA, USA.

ASTM (American Society for Testing and Materials). (2018). "Standard Test Methods and Definitions for Mechanical Testing of Steel Products." ASTM A370/A370M-18, West Conshohocken, PA, USA.

CSA (Canadian Standards Association). (2014). "Canadian Highway Bridge Design Code", CSA S6-14, Mississauga, Ontario, Canada.

CSA (Canadian Standards Association). (2017). “Design and construction of building structures with fiber-reinforced polymers.” CSA S806-12, Mississauga, Ontario, Canada.

CSA (Canadian Standards Association). (2019). “Canadian Highway Bridge Design Code” CSA S6-19, Mississauga, Ontario, Canada.

De Luca, A., Matta, F., and Nanni, A. (2010). “Behavior of Full-Scale Glass Fiber-Reinforced Polymer Reinforced Concrete Columns under Axial Load.” *ACI Structural Journal, 107*(5), 589-596.

Elchalakani, M., and Ma., G. (2017). “Tests of glass fibre reinforced polymer rectangular concrete columns subjected to concentric and eccentric axial loading.” *Engineering Structures, 151*, 93-104.

Elchalakani, M., Karrech, A., Dong, M., Alib, M., and Yang, B. (2018). “Experiments and Finite Element Analysis of GFRP Reinforced Geopolymer Concrete Rectangular Columns Subjected to Concentric and Eccentric Axial Loading.” *Structures, 14*, 273-289.

Elmessalami, N., El Refai, A., and Abed, F. (2019). “Fiber-reinforced polymers bars for compression reinforcement: a promising alternative to steel bars.” *Construction and Building Materials, 209*, 725-737.

Fib Bulletin 40. (2007). *FRP Reinforcement in RC structures.* Stuttgart: the International Federation for Structural Concrete.

Fillmore, B., and Sadeghian P. (2018) “Contribution of longitudinal glass fiber-reinforced polymer bars in concrete cylinders under axial compression.” *Canadian Journal of Civil Engineering,* 45(6): 458-468.Guérin, M., Mohamed, H. M., Benmokrane, B., Nanni, A., and Shield, C. K. (2018a). “Eccentric Behavior of Full-Scale Reinforced Concrete Columns with Glass Fiber-Reinforced Polymer Bars and Ties.” *ACI Structural Journal, 115*(2), 489-499.

Guérin, M., Mohamed, H. M., Benmokrane, B., Shield, C. K., and Nanni, A. (2018b). "Effect of glass fiber-reinforced polymer reinforcement ratio on axial-flexural strength of reinforced concrete columns." *ACI Structural Journal, 155*(4), 1049-3.

Hadhood, A., Mohamed, H. M., and Benmokrane, B. (2016). "Experimental study of circular high-strength concrete columns reinforced with GFRP bars and spirals under concentric and eccentric loading." *Journal of Composites for Construction, 21*(2), 04016078.

Hadhood, A., Mohamed, H. M., Benmokrane, B., Nanni, A., and Shield, C. K. (2019). "Assessment of Design Guidelines of Concrete Columns Reinforced with Glass Fiber-Reinforced Polymer Bars." *ACI Structural Journal, 116*(4), 193-207.

Hadi, M. N., Karim, H., and Sheikh, M. N. (2016). "Experimental investigations on circular concrete columns reinforced with GFRP bars and helices under different loading conditions." *Journal of Composites for Construction, 20*(4), 04016009.

Hales, T. A., Pantelides, C. P., and Reaveley, L. D. (2016). "Experimental evaluation of slender high-strength concrete columns with GFRP and hybrid reinforcement." *Journal of Composites for Construction, 20*(6), 04016050.

Hasan, H. A., Karim, H., Sheikh, M. N., and Hadi, M. N. (2019). "Moment-Curvature Behavior of Glass Fiber-Reinforced Polymer Bar-Reinforced Normal-Strength Concrete and High-Strength Concrete Columns." *ACI Structural Journal, 116*(4), 65-76.

Khorramian, K., and Sadeghian, P. (2017a). "Experimental and analytical behavior of short concrete columns reinforced with GFRP bars under eccentric loading." *Engineering Structures, 151*, 761–773.

Khorramian, K., and Sadeghian, P. (2017b). "Short Concrete Columns Reinforced with GFRP Rebars Under Eccentric Loading." *CSCE annual conference*, *Canadian Society for Civil Engineering*, Vancouver, Canada.

Khorramian, K., and Sadeghian, P. (2018). "New Testing Method of GFRP Bars in Compression." *CSCE Annual Conference*, *Canadian Society for Civil Engineering* (pp. MA7:1-9), Fredericton, NB, Canada.

Khorramian, K., and Sadeghian, P. (2019a). "Behavior of Slender GFRP Reinforced Concrete Columns." *ASCE-SEI Structures Congress, American Society of Civil Engineers*, St. Louis, Missouri, USA.

Khorramian, K., and Sadeghian, P. (2019b). "Material Characterization of GFRP Bars in Compression using a New Test Method." *Journal of Testing and Evaluation (ASTM)*, 49(2).

Maranan, G. B., Manalo, A. C., Benmokrane, B., Karunasena, W., and Mendis, P. (2016). "Behavior of concentrically loaded geopolymer-concrete circular columns reinforced longitudinally and transversely with GFRP bars." *Engineering Structures, 117*, 422-436.

Mirmiran, A., Yuan, W., and Chen, X. (2001). "Design of Slenderness in Concrete Columns Internally Reinforced with Fiber-Reinforced Polymer Bars." *ACI Structural Journal, 98*(1), 116-125.

Mirza, S. A. (1990). "Flexural Stiffness of Rectangular Reinforced Concrete Columns." *ACI Structural Journal, 87*(4), 425-435.

Mohamed, H. M., Afifi, M. Z., and Benmokrane, B. (2014). "Performance Evaluation of Concrete Columns Reinforced Longitudinally with FRP Bars and Confined with FRP Hoops and Spirals under Axial Load." *Journal of Bridge Engineering, 19*(7), 04014020.

Nanni, A., De Luca, A., and Zadeh, H. J. (2014). "Reinforced Concrete with FRP Bars: Mechanics and Design." *CRC Press*.

Pantelides, C. P., Gibbons, M. E., and Reaveley, L. D. (2013). "Axial load behavior of concrete columns confined with GFRP spirals." *Journal of Composites for Construction, 17*(3), 305-313.

Paultre, P., and Légeron, F. (2008). "Confinement reinforcement design for reinforced concrete columns." *Journal of structural engineering, 134*(5), 738-749.

Salah-Eldin, A., Mohamed, H. M., and Benmokrane, B. (2019). "Structural performance of high-strength-concrete columns reinforced with GFRP bars and ties subjected to eccentric loads." *Engineering Structures, 185*, 286-300.

Sun, L., Wei, M., and Zhang, N. (2017). "Experimental study on the behavior of GFRP reinforced concrete columns under eccentric axial load." *Construction and Building Materials, 152*, 214-225.

Tikka, T., Francis, M., & Teng, B. (2010, June). "Strength of Concrete Beam-Columns Reinforced with GFRP Bars." *2nd International structures specialty conference, Winnipeg, Manitoba*, 46.1-46.10.

Tobbi, H., Farghaly, A. S., and Benmokrane, B. (2012). "Concrete columns reinforced longitudinally and transversally with glass fiber-reinforced polymer bars." *ACI Structural Journal, 109*(4), 551-558.

Tobbi, H., Farghaly, A. S., and Benmokrane, B. (2014). "Behavior of Concentrically Loaded Fiber-Reinforced Polymer Reinforced Concrete Columns with Varying Reinforcement Types and Ratios." *ACI Structural Journal, 111*(2), 375-385.

Xue, W., Peng, F., and Fang, Z. (2018). “Behavior and Design of Slender Rectangular Concrete Columns Longitudinally Reinforced with Fiber-Reinforced Polymer Bars.” *ACI Structural Journal, 115*(2), 311-322.

Zadeh, H. J., and Nanni, A. (2013). “Design of RC columns using glass FRP reinforcement” *journal of composites for construction, 17*(3), 294-304.

Zadeh, H. J., and Nanni, A. (2017). “Flexural Stiffness and Second-Order Effects in Fiber-Reinforced Polymer-Reinforced Concrete Frames.” *ACI Structural Journal, 114*(2), 533-543.

NOTATION

The following symbols are used in this paper:

A_f = the cross-sectional area of longitudinal FRP reinforcement;

A_{fc} = area of GFRP bars in compression side;

A_{ft} = area of GFRP bars in the tensile side;

A_g = gross cross-sectional area of concrete;

A_{st} = the cross-sectional area of longitudinal steel reinforcement;

COV = coefficient of variation;

d_1 = the centroid of bars in the compression side;

d_2 = the centroid of bars in the tensile side;

d_C = the distance between the neutral axis and the resultant of the internal compressive forces of concrete;

d_{fc} = the distance between the neutral axis and the centroid of the compressive GFRP bars;

d_{ft} = the distance between the neutral axis and the centroid of the tensile GFRP bars;

e_0 = initial eccentricity;

E_c = modulus of elasticity of concrete;

E_f = modulus of elasticity of FRP bars;

E_{fc} = modulus of elasticity of GFRP bars in compression;

E_{ft} = modulus of elasticity of GFRP bars in tension;

E_s = modulus of elasticity of steel rebar;

EI = effective stiffness;

EI_D = experimental flexural stiffness corresponding to design strength (when the concrete reaches the design strain of 0.003 mm/mm per ACI 318-19);

EI_{GC} = experimental flexural stiffness corresponding to crushing of GFRP bars in compression;

EI_i = the calculated stiffness based on i^{th} equation provided in Table 6 (i =1 to 10);

EI_{peak} = experimental flexural stiffness corresponding to peak load;

EI_{SP} = experimental flexural stiffness corresponding to concrete spalling;

F_C = the resultant of internal forces of concrete in compression;

F_{fc} = the internal force of GFRP bars in compression;

F_{ft} = the internal force of GFRP bars in tension;

f'_c = compressive strength of concrete;

f'_{fcu} = ultimate crushing strength of GFRP bars in compression;

f'_{ftu} = ultimate rupture strength of GFRP bars in tension;

f'_y = yield strength of steel rebar;

h = the width of column cross-section;

I_f = moment of inertia of all GFRP bars in the concrete column;

I_g = moment of inertia of gross cross-section of concrete (chamfers are excluded);

I_s = moment of inertia of all steel bars in the concrete column;

k = Effective length factor (unbraced length) of the concrete columns;

l = The length of the column;

M = Bending moment ($M = P\times(e_0+\Delta)$);

M_C = internal moment resistance due to compressive concrete;

M_{CC} = the bending moment corresponding to concrete crushing;

M_D = the experimental moment at design load (when the concrete reaches the design strain of 0.003 mm/mm at the furthest concrete fiber in compression);

M_{D_1st} = the experimental first-order moment calculated at design load;

M_{fc} = internal moment resistance due to compressive GFRP bars;

M_{ft} = internal moment resistance due to tensile GFRP bars;

M_{GC} = the bending moment corresponding to crushing of GFRP bar in compression;

M_u = the moment capacity of the specimens at their peak load;

M_{ult} = the ultimate factored moment;

M_{u_1st} = the experimental first-order moment calculated at peak load;

n = modular ratio (the ratio of modulus of elasticity of GFRP bars to concrete);

P = axial load;

P_{CC} = the axial load corresponding to concrete crushing;

P_{cr} = critical buckling load;

P_D = design load (when the concrete reaches the design strain of 0.003 mm/mm at the furthest concrete fiber in compression);

P_{GC} = the axial load corresponding to crushing of GFRP bar in compression;

P_o = nominal axial strength at zero eccentricity;

P_u = the axial capacity of the specimens at their peak load;

P_{ult} = the ultimate factored load;

r = the radius of gyration;

STD = standard deviation;

$\varepsilon_{CC,c}$ = the compressive strain of GFRP bar in compression side corresponding to crushing of concrete;

ε_{fcu} = the ultimate crushing strain of GFRP bars in compression;

ε_{fc} = the strain of GFRP bars in compression;

ε_{ftu} = the ultimate rupture strain of GFRP bars in tension;

ε_{ft} = the strain of GFRP bars in tension;

$\varepsilon_{GC,c}$ = the compressive strain of GFRP bar in compression side corresponding to crushing of GFRP bars in compression;

$\varepsilon_{peak,c}$ = the compressive strain of GFRP bar in compression side corresponding to peak load;

ε_y = yield strain of steel rebar;

δ = moment magnification factor;

δ_{calc} = calculated moment magnification factor;

δ_{test} = experimental moment magnification factor;

Δ = lateral displacement at mid-span;

Δ_{axial} = the axial displacement of the specimens at their peak load;

Δ_{CC} = the lateral displacement corresponding to concrete crushing;

Δ_{GC} = the lateral displacement corresponding to crushing of GFRP bar in compression;

$\Delta_{lateral}$ = the lateral displacement of the specimens at their peak load;

λ = slenderness ratio;

ρ = reinforcement ratio;

ψ = the curvature of the column at the mid-section.

Table 1. Test matrix.

No.	Specimen ID	λ	*e/h*	ρ (%)	Class
1	G17-e23-r4-N1	16.6	0.23	4.80	GFRP
2	G17-e23-r4-N2	16.6	0.23	4.80	GFRP
3	G22-e23-r4-N1	21.5	0.23	4.80	GFRP
4	G22-e21-r4-N2	21.5	0.21	4.80	GFRP
5	S22-e23-r2-N3	21.5	0.23	1.00	Steel
7	G40-e23-r2-N1	39.7	0.23	2.87	GFRP
9	G40-e23-r4-N2	39.7	0.23	4.80	GFRP
6	G40-e21-r2-N3	39.7	0.21	2.87	GFRP
8	G40-e21-r4-N4	39.7	0.21	4.80	GFRP
10	G60-e23-r4-N1	59.5	0.23	4.80	GFRP

Note: Class = reinforcement type.

Table 2. Summary of material properties.

Test Type	Material	Strength / Yielding		Modulus of elasticity		Ultimate / Yield strain	
		Symbol	(MPa)	*Symbol*	(GPa)	*Symbol*	(mm/mm)
Compression	Concrete	f'_c	56.8 ± 1.9	E_c	35.0 ± 1.2		-
	#6 GFRP bar	f'_{fcu}	684.2 ± 33.1	E_{fc}	48.9 ± 0.9	ε_{fcu}	0.0140
Tension	#3 GFRP bar	$*f'_{ftu}$	827	$*E_{ft}$	46	$*\varepsilon_{ftu}$	0.0179
	#6 GFRP bar	f'_{ftu}	963.0 ± 62.1	E_{ft}	43.4 ± 0.9	ε_{ftu}	0.0222
	Steel rebar	f'_y	442.6 ± 4.7	E_s	209.4 ± 5.6	ε_y	0.0021

Note: * = guaranteed values reported by the manufacturer per ASTM D7205 (2016). It should be mentioned that guaranteed means the average for modulus of elasticity and an average minus three times the standard deviation for tensile strength per ACI 440.1R-15 (2015).

Table 3. Summary of test results.

Group	No.	Specimen ID	P_u (kN)	Δ_{axial} (mm)	$\Delta_{lateral}$ (mm)	M_u (kN-m)	d_1 (mm)	d_2 (mm)
Short Columns	1	G17-e23-r4-N1	1401	21	11	80.8	60	150
	2	G17-e23-r4-N2	1480	18	7	80.1	54	149
	3	G22-e23-r4-N1	1550	17	8	84.7	54	150
	4	G22-e21-r4-N2	1410	18	9	73.4	53	148
	5	S22-e23-r2-N3	1564	17	9	87.4	47	150
Slender Columns	6	G40-e23-r2-N1	1210	22	22	83.8	58	150
	7	G40-e23-r4-N2	1116	16	23	78.8	52	154
	8	G40-e21-r2-N3	1204	17	24	78.4	53	154
	9	G40-e21-r4-N4	1315	17	23	87.1	55	144
	10	G60-e23-r4-N1	844	17	34	69.6	58	150

Table 4. Axial load, bending moment, and lateral displacement capacities of columns after concrete crushing up to failure.

No.	Specimen ID	P_{CC} (kN)	P_{GC} (kN)	Load drop (%)	M_{CC} (kN-m)	M_{GC} (kN-m)	Moment drop (%)	Δ_{CC} (mm)	Δ_{GC} (mm)	Δ_{CC} - Δ_{GC} (mm)
1	G17-e23-r4-N2	1466	1140	-22.2	80.0	82.7	3.3	7	25	18
2	G22-e23-r4-N1	1544	930	-39.8	85.1	73.0	-14.2	8	29	21
3	G22-e21-r4-N2	1403	900	-35.9	73.5	67.2	-8.7	10	31	21
4	S22-e23-r2-N3	1489	NA	NA	83.5	NA	NA	9	NA	NA
6	G40-e23-r2-N1	1205	421	-65.1	87.7	62.8	-28.4	25	85	60
8	G40-e23-r4-N2	1108	536	-51.6	80.5	76.3	-5.2	25	82	57
5	G40-e21-r2-N3	1201	449	-62.6	82.0	59.1	-27.9	26	74	48
7	G40-e21-r4-N4	1281	504	-60.7	89.1	93.3	4.7	27	143	116
9*	G60-e23-r4-N1	712	353	-50.4	84.0	85.3	1.4	44	194	150
Average				-48.5			-10			61
STD				14.0			12			45
COV				-28.8			-132			74

Note: * = test stopped before crushing of GFRP bar due to excessive deformation.

Table 5. The compressive strain of GFRP/steel bars at different loading stages.

No.	Specimen ID	SG2 (mm/mm)				SG4 (mm/mm)			
		$\varepsilon_{peak,c}$	$\varepsilon_{CC,c}$	$\varepsilon_{GC,c}$	$\varepsilon_{GC,c}$ - $\varepsilon_{CC,c}$	$\varepsilon_{peak,c}$	$\varepsilon_{CC,c}$	$\varepsilon_{GC,c}$	$\varepsilon_{GC,c}$ - $\varepsilon_{CC,c}$
1	G17-e23-r4-N2	-0.0041	-0.0049	-0.0150	-0.0101	-0.0023	-0.0024	NA	NA
2	G22-e23-r4-N1	-0.0023	-0.0025	NA	NA	-0.0030	-0.0033	NA	NA
3	G22-e21-r4-N2	-0.0022	-0.0023	-0.0103	-0.0080	-0.0028	-0.0030	NA	NA
4	S22-e23-r2-N3	-0.0039	-0.0039	NA	NA	-0.0018	-0.0018	NA	NA
5	G40-e23-r2-N1	-0.0020	-0.0025	-0.0103	-0.0078	-0.0024	-0.0029	-0.0100	-0.0071
6	G40-e23-r4-N2	-0.0022	-0.0023	-0.0052	-0.0029	-0.0030	-0.0034	-0.0140	-0.0107
7	G40-e21-r2-N3	-0.0020	-0.0037	NA	NA	-0.0028	-0.0041	NA	NA
8	G40-e21-r4-N4	-0.0016	-0.0018	-0.0068	-0.0050	-0.0029	-0.0072	NA	NA
9*	G60-e23-r4-N1	-0.0010	-0.0016	NA	NA	-0.0011	-0.0018	-0.0055	-0.0037
Average					-0.0068				-0.0072
STD					0.0025				0.0028
COV					-37.6				-39.4

Note: * = test stopped before crushing of GFRP bar due to excessive deformation.

Table 6. Reference for the equations in the literature for calculating flexural stiffness of RC columns.

No. Flexural stiffness equation number	Reference
(1)	(ACI 318-19, 2019) (6.6.4.4.4a)
(2)	(ACI 318-19, 2019) (6.6.4.4.4b)
(3)	(ACI 318-19, 2019) (6.6.4.4.4a) And (Table 6.6.3.1.1b)
(4)	(Mirza, 1990)
(5)	(Mirza, 1990)
(6)	(Mirmiran et al., 2001)
(7)	(Mirmiran et al., 2001)
(8)	(Zadeh and Nanni, 2013)
(9)	(Zadeh and Nanni, 2017)
(10)	(Xue et al., 2018)

Note: All formulas have been normalized to 0.75 to have the same stiffness reduction factor per ACI 318-19 (2019).

Table 7. The flexural stiffness of test specimens at different loading stages in comparison with values obtained from the literature.

No.	Specimen ID	Flexural stiffness, EI (kN-m^2)													
		At loading stages of Fig. 13				From the literature (See Table 6)									
		EI_{peak}	EI_D	EI_{SP}	EI_{GC}	EI_1	EI_2	EI_3	EI_4	EI_5	EI_6	EI_7	EI_8	EI_9	EI_{10}
1	G17-e23-r4-N2	2232	1864	1864	429	2748	1652	6012	1644	1741	776	602	6012	1583	1852
2	G22-e23-r4-N1	2960	2497	2633	288	2748	1661	6012	1680	1749	780	606	6012	1589	1914
3	G22-e21-r4-N2	1968	2086	1853	225	2748	1655	6012	1714	1782	791	604	6012	1585	2045
4	S22-e23-r2-N3	1543	NA	1788	NA	2748	1694	6012	1711	1780	1295	1217	6012	1614	1945
6	G40-e23-r2-N1	2247	2433	1675	186	2748	1539	6012	1672	1635	723	561	5690	1498	2000
8	G40-e23-r4-N2	1870	2096	1675	188	2748	1697	6012	1819	1783	797	619	6012	1616	2147
5	G40-e21-r2-N3	2241	2110	1355	463	2748	1563	6012	1732	1696	746	570	5691	1516	2165
7	G40-e21-r4-N4	3465	2744	2729	397	2748	1624	6012	1790	1753	776	592	6012	1561	2222
9*	G60-e23-r4-N1	3135	2583	1468	511	2748	1637	6012	1877	1726	769	597	6012	1571	2308
Average		2407	2302	1893	336	2748	1636	6012	1738	1738	828	663	5940	1570	2066
STD		603	285	450	121	0	51	0	72	45	166	197	133	38	145
COV (%)		25	12	24	36	0	3	0	4	3	20	30	2	2	7

Note: * = test stopped before crushing of GFRP bar due to excessive deformation.

Table 8. Moment magnification factor at the design load level and at the peak load.

No.	Specimen ID	At the design strain of 0.003 mm/mm**						At the peak load			
		P_D (kN)	M_D (kN-m)	M_{D_1st} (kN-m)	δ_{calc}	δ_{test}	$\delta_{calc}/\delta_{test}$	M_{u_1st} (kN-m)	δ_{calc}	δ_{test}	$\delta_{calc}/\delta_{test}$
1	G17-e23-r4-N2	1472	80.0	69.2	1.10	1.16	0.95	69.6	1.09	1.15	0.94
2	G22-e23-r4-N1	1546	84.0	72.6	1.13	1.16	0.98	72.9	1.11	1.16	0.95
3	G22-e21-r4-N2	1403	72.5	60.3	1.15	1.20	0.95	60.6	1.16	1.21	0.95
4	S22-e23-r2-N3	NA	NA	NA	NA	NA	NA	73.5	1.24	1.19	1.04
6	G40-e23-r2-N1	1206	81.8	56.7	1.41	1.44	0.98	56.9	1.46	1.47	0.99
8	G40-e23-r4-N2	1101	74.0	51.8	1.45	1.43	1.01	52.5	1.54	1.50	1.03
5	G40-e21-r2-N3	1203	79.6	51.7	1.50	1.54	0.98	51.8	1.46	1.51	0.96
7	G40-e21-r4-N4	1302	89.5	56.0	1.39	1.60	0.87	56.6	1.29	1.54	0.84
9	G60-e23-r4-N1	830	75.6	39.0	1.69	1.94	0.87	39.7	1.52	1.76	0.87
Average*		1258	79.6	57.2	1.35	1.43	0.95	79.6	1.33	1.41	0.94
STD*		228	5.6	10.6	0.21	0.27	0.05	5.6	0.19	0.22	0.06
COV (%) *		18	7	19	15	19	5	7	14	15	7

Note: * = The steel-RC column is excluded in the calculation of average, standard deviation, and coefficient of variation; ** = the furthest compressive fiber in concrete reached a design strain of 0.003 mm/mm; The loads and moments corresponding to peak load were presented in Table 3.

Table 9. Calculated internal forces and moments at peak load and at GFRP bar crushing.

No.	Specimen ID	Contribution at peak load					Contribution at GC (GFRP bar crushing)				
		F_{fc} (kN)	F_C (kN)	M_{fc} (kN-m)	M_{ft} (kN-m)	M_C (kN-m)	F_{fc} (kN)	F_C (kN)	M_{fc} (kN-m)	M_{ft} (kN-m)	M_C (kN-m)
1	G17-e23-r4-N2	222	1293	17.9	0.5	61.7	1044	685	60.5	21.7	0.5
2	G22-e23-r4-N1	183	1399	14.7	0.5	69.5	NA	NA	NA	NA	NA
3	G22-e21-r4-N2	176	1318	10.9	2.8	59.7	719	865	33.1	33.7	0.4
4	S22-e23-r2-N3	133	1505	9.6	2.2	75.5	NA	NA	NA	NA	NA
5	G40-e21-r2-N1	93	1170	5.3	2.0	76.5	420	445	18.1	22.8	22.0
6	G40-e23-r4-N2	182	1041	11.2	4.4	63.2	359	681	14.2	31.5	30.5
7	G40-e21-r2-N3	101	1141	7.1	1.2	70.1	NA	NA	NA	NA	NA
8	G40-e21-r4-N4	154	1207	10.4	1.0	75.7	472	712	16.1	37.7	39.4
9	G60-e23-r4-N1	75	834	3.5	2.9	63.2	384	642	11.9	41.2	32.2

Note: NA = not available.

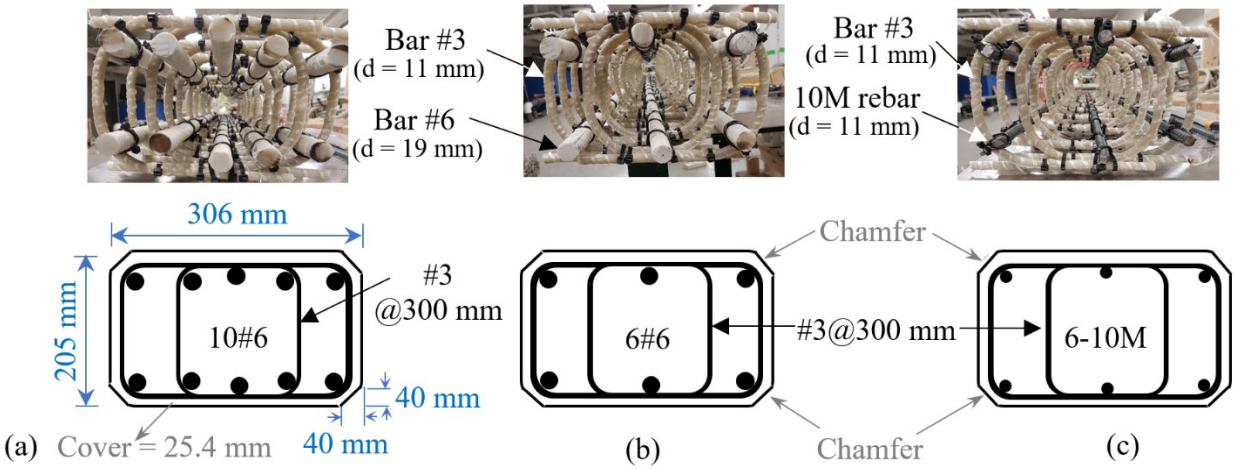

Fig. 1. Rebar layout: (a) GFRP-RC column with 4.80 % reinforcement ratio; (b) GFRP-RC column with 2.87% reinforcement ratio; (c) steel RC column with 1.00% reinforcement ratio.

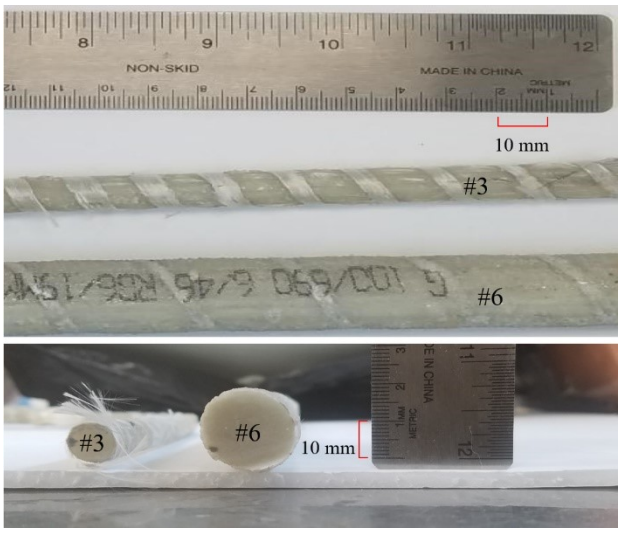

Fig. 2. Bar size and bar cross-sections.

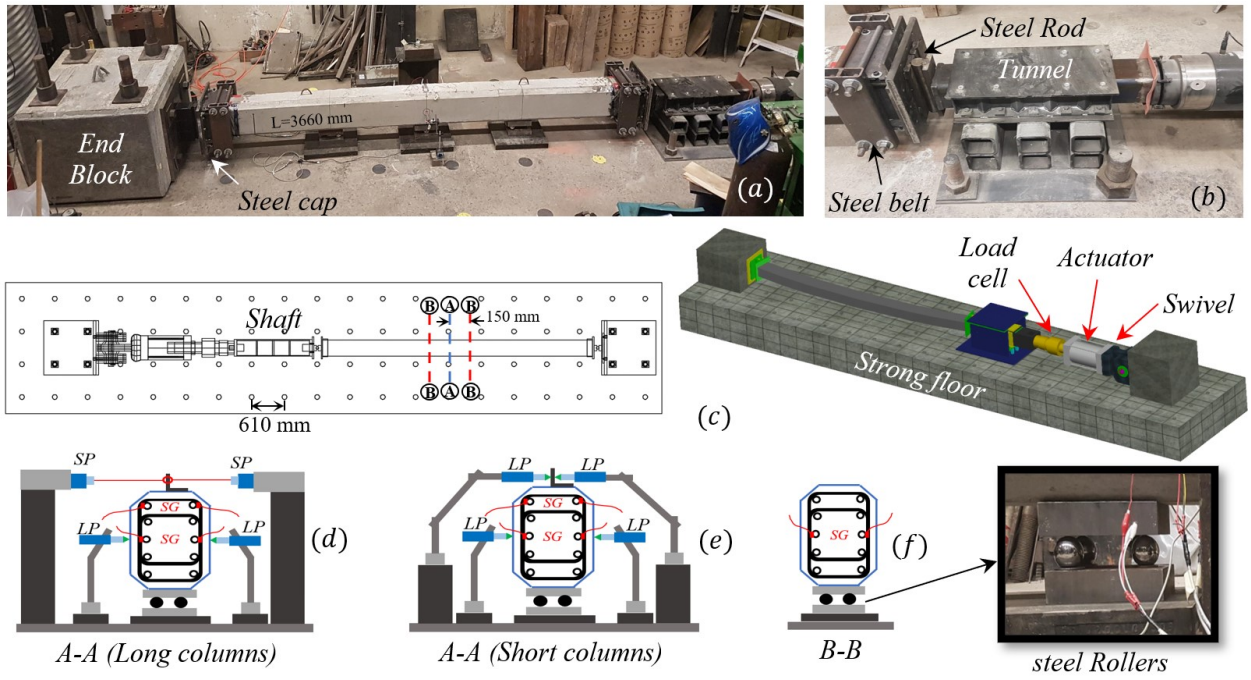

Fig. 3. Test set up and instrumentation: (a) test-set up for slender columns; (b) loading detail; (c) schematic test set-up; (d) location of LPs and SPs for long column test set-up; (e) location of LPs for short column test set-up; and (f) strain gauging of sections far from center.

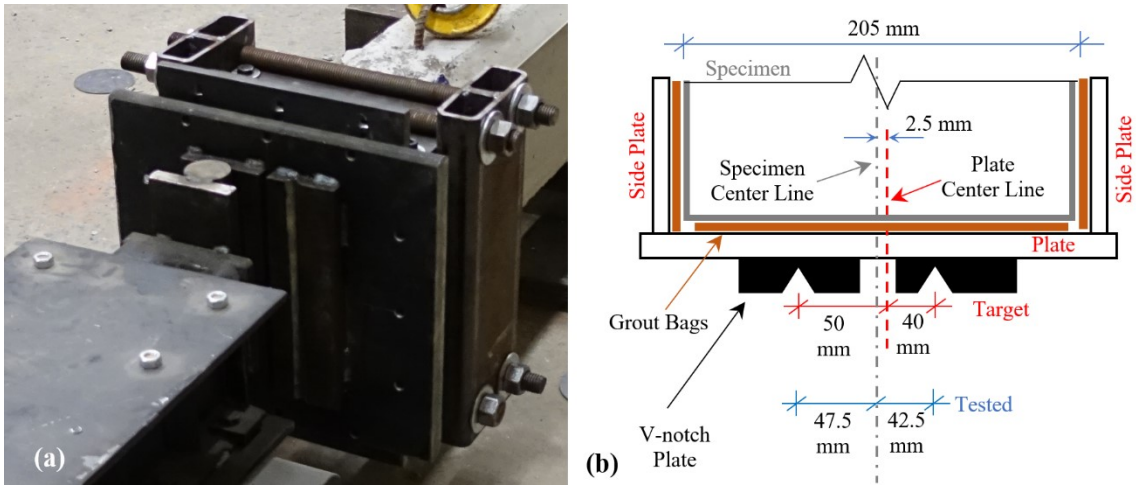

Fig. 4. Steel fixture at each end to apply eccentric loading: (a) photo and (b) schematic drawing.

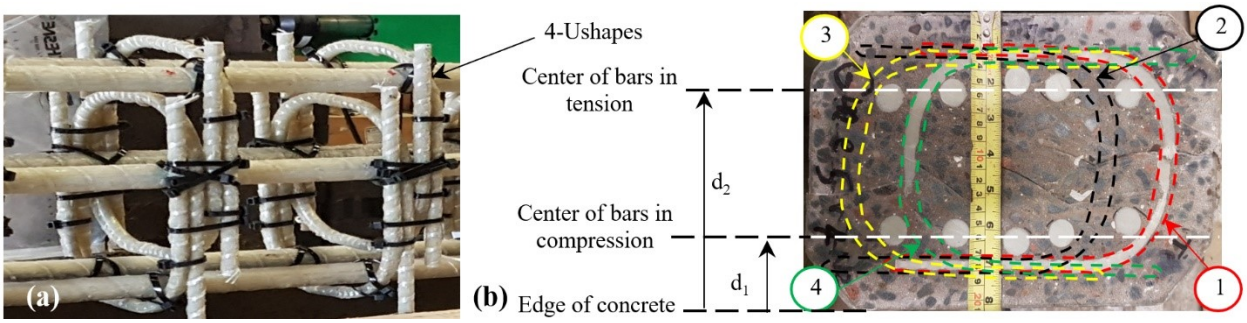

Fig. 5. Transverse reinforcement and bar locations: (a) ties; and (b) location of bars.

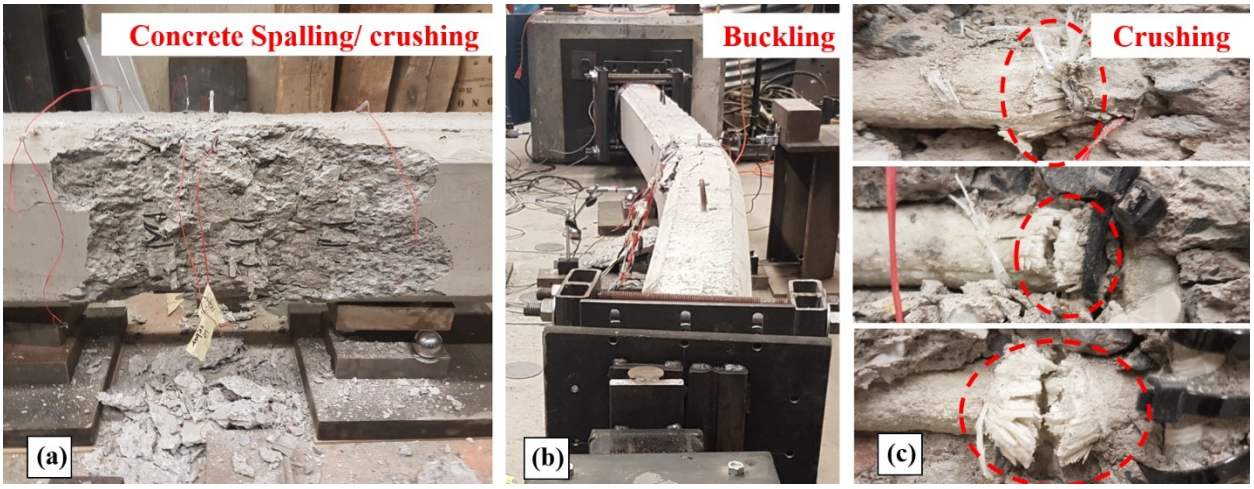

Fig. 6. Failure modes: (a) concrete crushing/ spalling (CC); (b) global buckling (GB); and (c) GFRP crushing (GC).

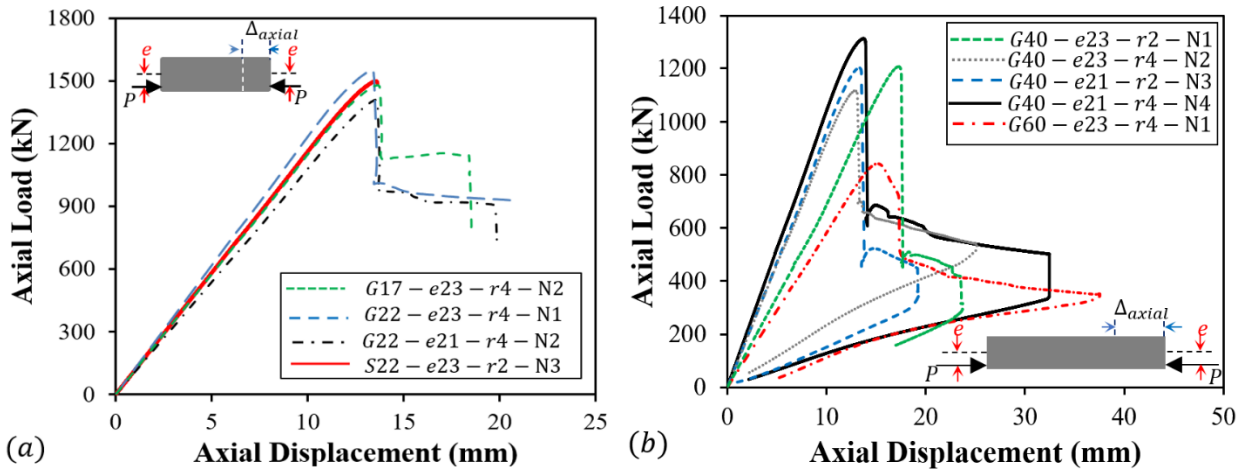

Fig. 7. Axial load-axial displacement curves: (a) short columns; and (b) slender columns.

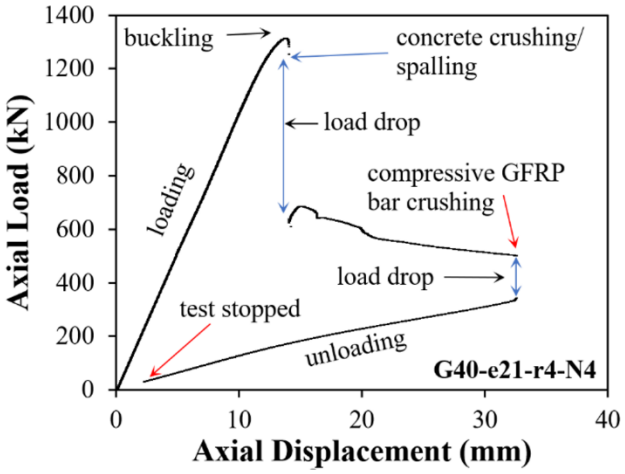

Fig. 8. loading stages of slender GFRP RC columns.

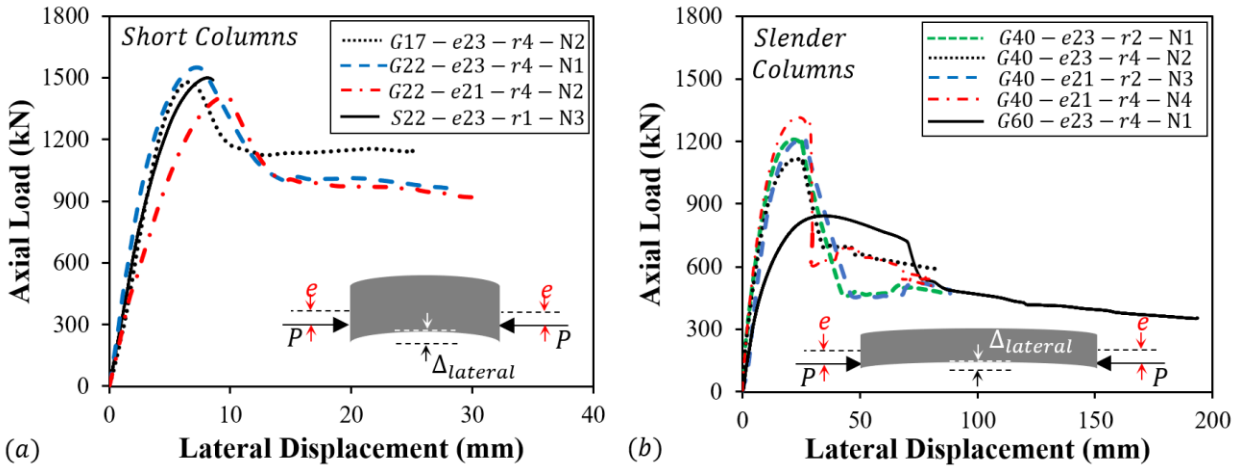

Fig. 9. Axial load- lateral displacement curves for: (a) short columns; and (b) slender columns.

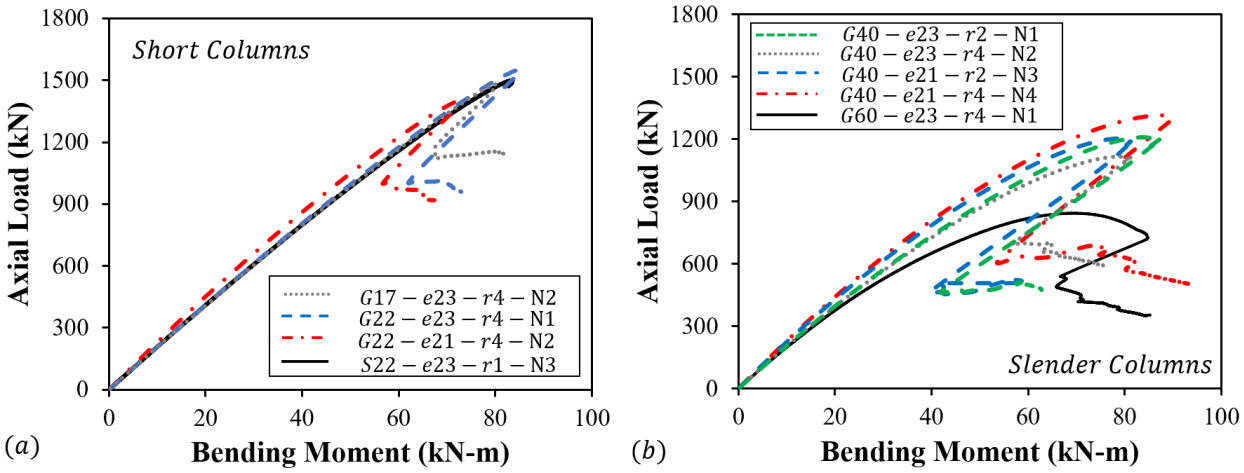

Fig. 10. Axial load- bending moment curves for: (a)short columns; and (b)slender columns.

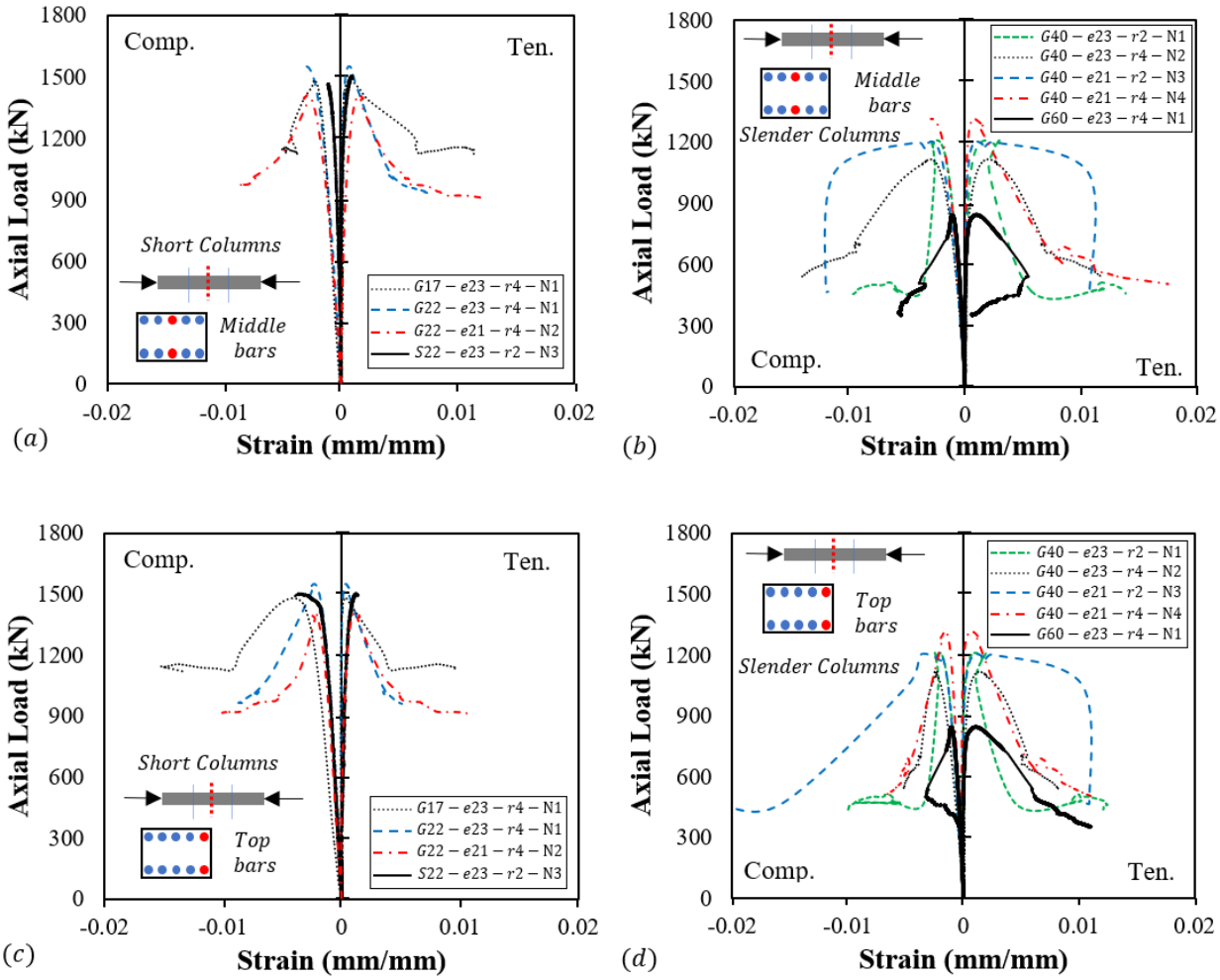

Fig. 11. The axial load-axial strain of GFRP bars for: (a)short columns at middle bars; (b)slender columns at middle bars; (c) short columns at top bars; and (d) slender columns at top bars.

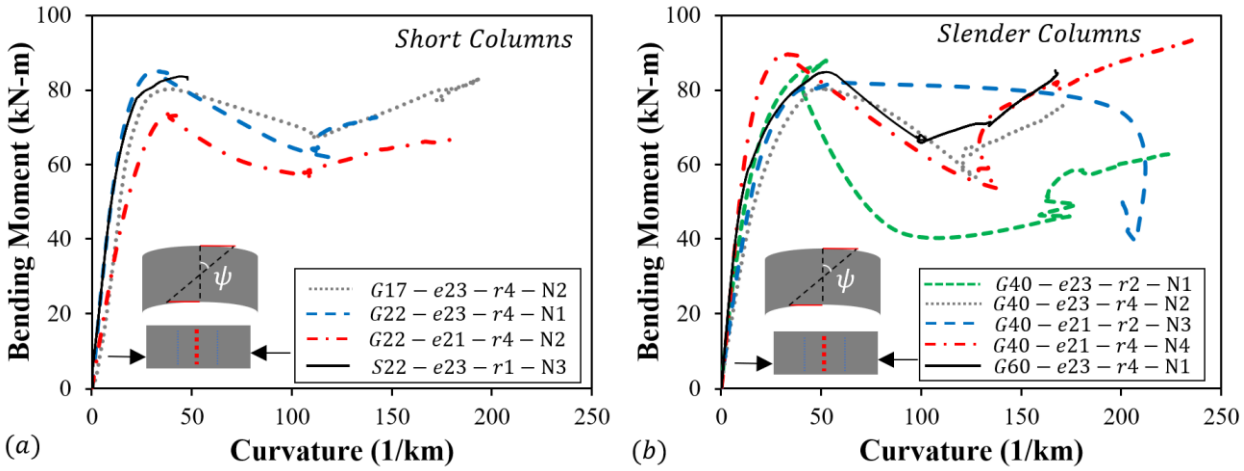

Fig. 12. Moment-curvature curves for: (a) short columns; and (b) slender columns.

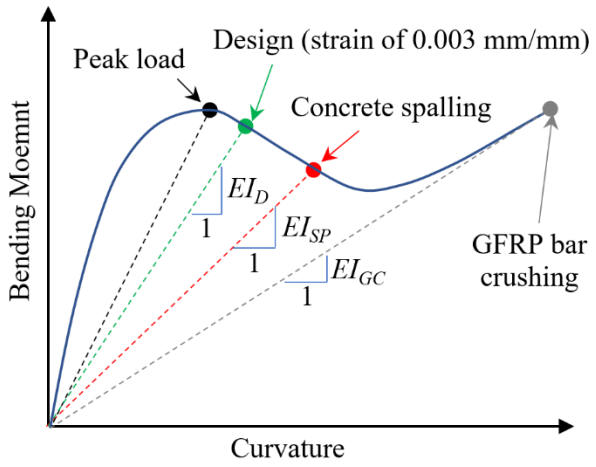

Fig. 13. Calculation of flexural stiffness at different loading stages.

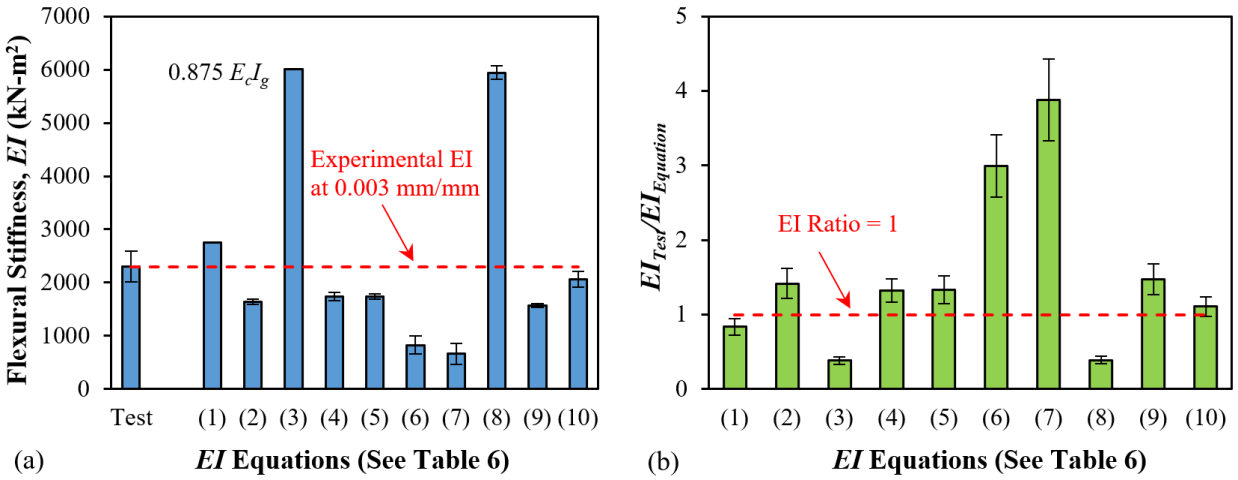

Fig. 14. Comparison of flexural stiffness obtained from the current experimental program and major equations from the literature: (a) *EI* values; and (b) *EI* ratios.

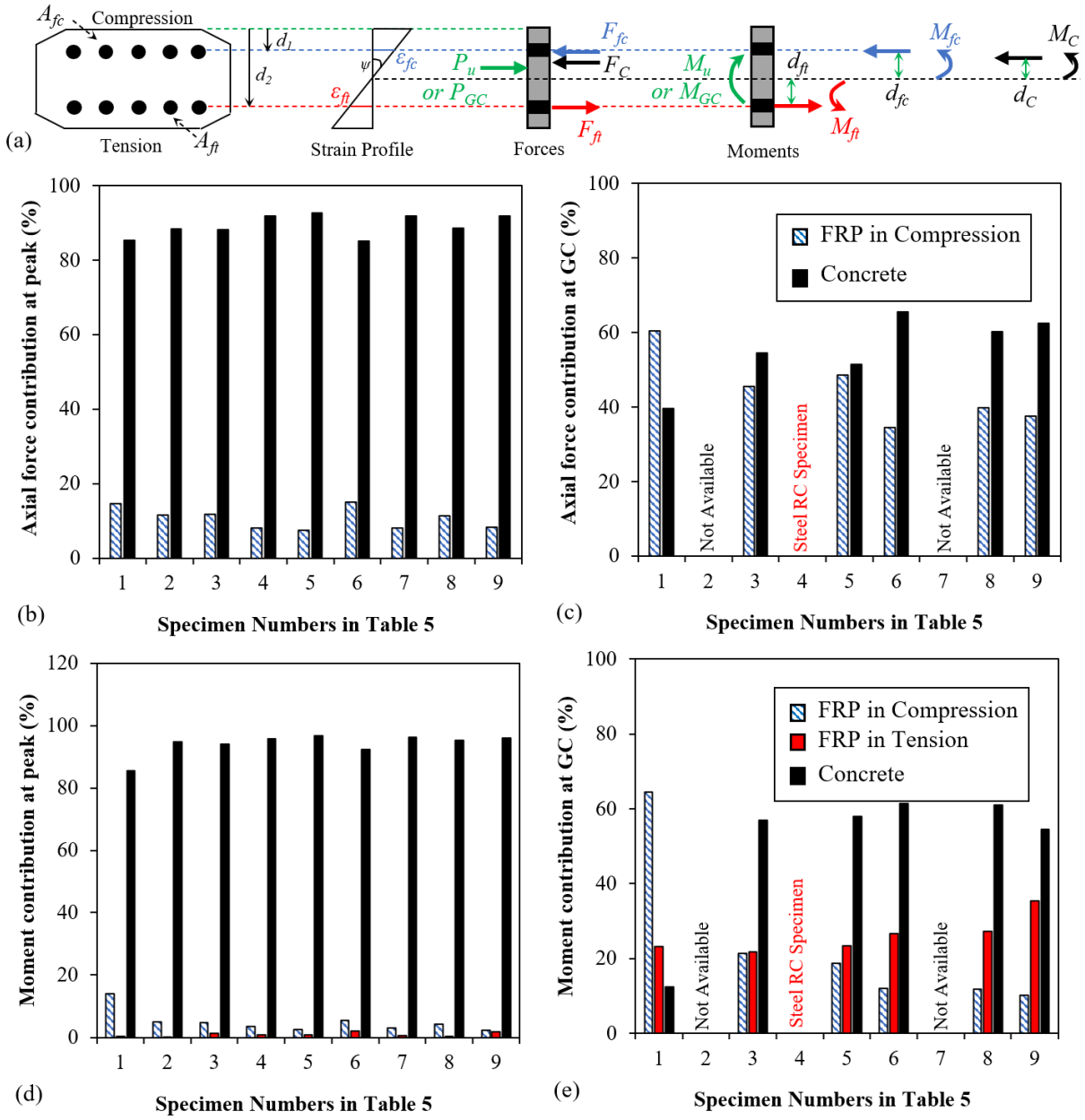

Fig. 15. Contribution of GFRP bars: (a) illustration of calculations; (b) axial force contribution at peak load; (c) axial force contribution at compressive GFRP bar crushing; (d) bending moment contribution at peak load; (e) bending moment contribution at compressive GFRP bar crushing.

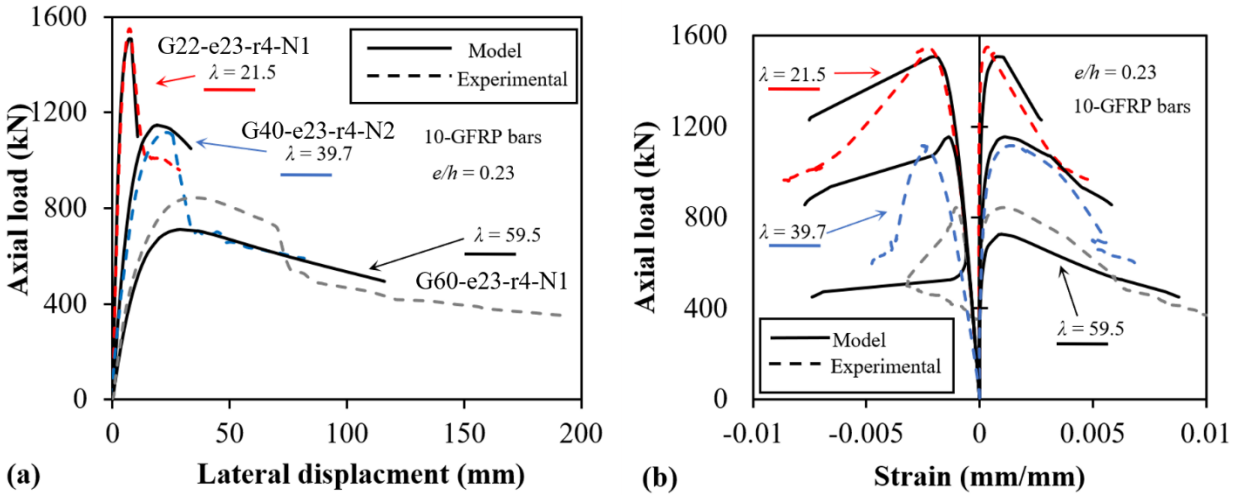

Fig. 16. Verification: (a) load-displacement curves; and (b) load-strain curves.

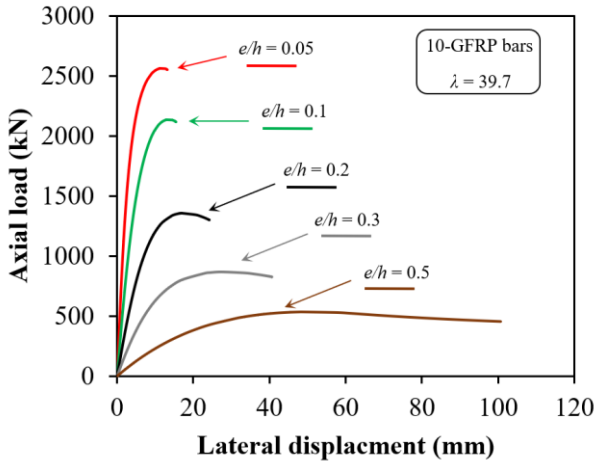

Fig. 17. Parametric Study on eccentricity effect.